The Random Line-of-Sight Over-the-Air Measurement System

MADELEINE SCHILLIGER KILDAL

CHALMERS

Department of Electrical Engineering
Antenna Systems
CHALMERS UNIVERSITY OF TECHNOLOGY

Göteborg, Sweden 2020

The Random Line-of-Sight Over-the-Air

Measurement System

Madeleine Schilliger Kildal

ISBN 978-91-7905-296-6

Department of Electrical Engineering
Antenna Systems
Chalmers University of Technology
SE–412 96 Göteborg
Sweden
Telephone: +46 (0)31 – 772 1000
Email: madeleine.kildal@chalmers.se; madeleine@kildal.se

Front Cover: The random line-of-sight sub-6 GHz solution.

Till pappa

Abstract

As our society becomes increasingly connected, a growing number of devices rely on wireless connectivity. The type, use and form factor of these devices range from wearables to entire vehicles. Additionally, the fifth generation of wireless communication (5G) introduces new communication bands, also at higher frequencies. At these millimeter-wave frequencies, large portions of bandwidth are available which are needed in order to increase the data rates.

In this scenario, testing and verifying the wireless communication performance has an increasingly important role. In modern devices, testing needs to be performed over-the-air (OTA), as direct conducted measurements to the antenna ports become unfeasible. Moreover, there is still ongoing research to understand how testing should be performed for devices with large form-factors, such as vehicles, as well as for higher frequencies. The proposed methods are mainly based on techniques for mobile phone testing at the current communication bands, i.e., sub-6 GHz. However, scaling and adapting these methods to work for future needs presents challenges.

A possible solution to meet the future testing requirements is offered by the following hypothesis: *"If a wireless device is tested with good performance in both pure-LOS and RIMP environments, it will also perform well in real-life environments and situations, in a statistical sense"*. The rich isotropic multipath (RIMP) and the random line-of-sight (random-LOS) are therefore identified as the two representative edge environments for testing. This thesis focuses on the random-LOS environment, and its practical realization to test the wireless performance of different devices.

The thesis is divided into three main parts. The first part describes the practical realization of random-LOS OTA measurement setups. Three different setups are presented, a virtual planar array and two reflector antennas. One reflector system is aimed at vehicular testing for frequencies below 6 GHz, while the other targets smaller devices at 28 GHz.

The second part of the thesis focuses on numerical and experimental verification of the random-LOS measurement setups. In the verification, numerical simulations and measurements of the test zone variations are compared for the proposed OTA measurement systems.

The third and last part focuses on how passive and active measurements can be performed using a random-LOS measurement setup. The measurements demonstrate the application of the designed OTA measurement systems for passive antenna

measurements, as well as active 2×2 multiple-input multiple-output (MIMO) measurements on a complete vehicle.

Preface

This thesis is in partial fulfillment for the degree of Doctor of Philosophy at Chalmers University of Technology, Gothenburg, Sweden.

The work resulting in this thesis was carried out between September 2014 and May 2020 in the Antenna Systems group, Division of Communications, Antennas, and Optical Networks at the Department of Electrical Engineering, Chalmers. Adjunct Professor Jan Carlsson has been the main supervisor and Associate Professor Andrés Alayón Glazunov together with Professor Jian Yang have been the co-supervisors. Professor Thomas Eriksson has been the examiner.

Acknowledgment

After years of work, resulting in this thesis, I am now at the end. These years have been an emotional roller coaster with struggles I never could have imagined, but also containing some of the nicest moments of my life, which I will bring with me forever. Thanks to all the supporting people around me, I have managed to conclude this thesis, which sometimes has felt like an impossible task. I would now like to thank those of you that have had a special part in my work towards this thesis.

First I would like to thank my main supervisor Adjunct Professor Jan Carlsson, for your great support, encouragement and guidance. Especially I would like to thank you for always being there for me, just a phone call away, when I need a discussion partner and have the most silly questions. I also want to thank my co-supervisor Associate Professor Andrés Alayón Glazunov for the time and interest you have put into my work. A thank also goes to my other co-supervisor Professor Jian Yang, for being a good discussion partner and for seeing my work from a different perspective. A special thanks goes to Professor Thomas Eriksson for examining this thesis.

I would like to thank Lars Granbom, for believing so much in me and generously including me in so many different exciting tasks. Thank you Lars-Inge Sjöqvist for always looking on the bright side of everything. I would also like to thank Bluetest, and especially John Kvarnstrand and Kjell Olovsson, for supporting me in difficult times and helping me to make the best of the situation. And to all the rest of you at Bluetest, thanks for welcoming me even though I was only at the office once a week. I would also like to thank Björn Bergqvist and Amir Majidzadeh for helping with the practicalities regarding the measurements at Volvo.

I would like to thank all the colleagues at the department of Electrical Engineering and the Antenna group. A special thanks to the extended antenna family with Abbas, Abolfazl, Ahmed, Aidin, Astrid, Jinlin, Oleg, Parastoo, Pegah, Sadegh, Samar, Tomas and Wan-Chun. You have made everything easier, have been there through the hard times and have always made me laugh. A super thanks goes to Carlo, Sadegh and Wan-Chun for proof-reading this thesis.

To Linnea, the best friend one could ever have. I don't know how many times I have called you the last months to update you about this thesis. Because you are the one I want to tell things, independent if it is something fun, if I am down or if I want you to decide what we should eat for dinner. Josefin, the best puzzle partner in the world, we have experienced so many things together and I am looking forward

to the future and all the amazing things that are to come. Sten, even if it can go a long time between we meet, it feels like no time has past at all and we can so easy catch up from where we left off. And a thanks to the rest of you, you know who you are, I am so lucky to have all of you wonderful people in my life.

Thank you amazing Carlo. You have been my greatest support throughout the work towards this thesis. So many things have happened these years, and you have been there all along. I don't know what I would have done without you. You always know how to make me laugh, how to push me so that I challenge myself, but also know when a hug is the best medicine in the world. Everything is easier with you. You are home to me.

To mum and Susanne. You are closest to my heart and mean the world to me. We have managed things together we didn't think were possible. We are a unit that can stand through anything.

To dad, I know you will read this somewhere, and I know you will be proud that I managed to finish this. I am so happy that I started doing my PhD in your group, that I got to see your love and passion for your work every day, that I got to be a part of it, that I got to share it too. You have opened a fascinating world to me, and you inspire me every day. You will always be in my heart.

Madeleine
Göteborg, May 2020

List of Publications

This thesis is based on the work contained in the following appended papers:

[A] **M.S. Kildal**, J. Carlsson, and A.A. Glazunov, "Measurements and Simulations for Validation of the Random-LOS Measurement Accuracy for Vehicular Applications", in *IEEE Transactions on Antennas and Propagation*, vol. 66, no. 11, pp. 6291-6299, November 2018.

[B] **M.S. Kildal**, S.M. Moghaddam, A. Razavi, J. Carlsson, J. Yang, and A.A. Glazunov, "Verification of the Random Line-of-Sight Measurement Setup at 1.5–3 GHz Including MIMO Throughput Measurements of a Complete Vehicle", submitted to *IEEE Transactions on Vehicular Technology*, May 2020.

[C] **M.S. Kildal**, S.M. Moghaddam, J. Carlsson, J. Yang, and A.A. Glazunov, "Evaluation of a Random Line-of-Sight Over-the-Air Measurement Setup at 28 GHz", submitted to *IEEE Transactions on Antennas and Propagation*, March 2020.

[D] **M.S. Kildal**, A.A. Glazunov, and J. Carlsson, "A Numerical Analysis of the Random-LOS Measurement Accuracy for Vehicle Applications", in *2018 12th European Conference on Antennas and Propagation (EuCAP)*, 9–13 April 2018, London, U.K.

[E] **M.S. Kildal**, A. Razavi, J. Carlsson, and A.A. Glazunov, "Test Zone Verification Procedures in a Random-LOS Measurement Setup", in *2019 13th European Conference on Antennas and Propagation (EuCAP)*, 31 March – 5 April 2019, Krakow, Poland.

Other related publications by the Author not included in this thesis:

[a] **M.S. Kildal**, X. Chen, P.-S. Kildal, and J. Carlsson, "Investigation of Mode Stirring with Plate on Platform in a Reverberation Chamber", in *2015 9th European Conference on Antennas and Propagation (EuCAP)*, 12–17 April 2015, Lisbon, Portugal.

[b] A.A. Glazunov, P.-S. Kildal, J. Carlsson, **M.S. Kildal**, and S. Mansouri, "Impact of the Spatial User Distribution on the Coverage Antenna Pattern of Maximum Ratio Combining in Random Line-of-Sight", in *2015 9th European Conference on Antennas and Propagation (EuCAP)*, 12–17 April 2015, Lisbon, Portugal.

[c] **M.S. Kildal**, J. Kvarnstrand, J. Carlsson, A.A. Glazunov, A. Majidzadeh, and P.-G. Kildal, "Initial Measured OTA Throughput of 4G LTE Communication to Cars with Roof-Mounted Antennas in 2D Random-LOS", in *2015 International Symposium on Antennas and Propagation (ISAP)*, 9–12 November 2015, Hobart, Australia.

[d] A.A. Glazunov, P.-S. Kildal, and **M.S. Kildal**, "Devising a Horizontal Chamber Array for Automotive OTA Tests in Random Line-Of-Sight", in *2015 International Symposium on Antennas and Propagation (ISAP)*, 9–12 November 2015, Hobart, Australia.

[e] **M.S. Kildal**, A.A. Glazunov, J. Carlsson, J. Kvarnstrand, A. Majidzadeh, and P.-S. Kildal, "Measured Probabilities of Detection for 1- and 2 Bitstreams of 2-port Car-roof Antenna in RIMP and Random-LOS", in *2016 10th European Conference on Antennas and Propagation (EuCAP)*, 10–15 April 2016, Davos, Switzerland.

[f] J. Kvarnstrand, S.S. Kildal, A. Skårbratt, and **M.S. Kildal**, "Comparison of Live Person Test to Head and Hand Phantom Test in Reverberation Chamber", in *2016 10th European Conference on Antennas and Propagation (EuCAP)*, 10–15 April 2016, Davos, Switzerland.

[g] **M.S. Kildal**, J. Carlsson, A.A. Glazunov, and P.-S. Kildal, "Measured LTE Throughput for SISO, SIMO and MIMO in Polarization-Random-LOS", in *2016 IEEE International Symposium on Antennas and Propagation (APSURSI)*, 26 June – 1 July 2016, Fajardo, Puerto Rico.

[h] **M.S. Kildal**, A.A. Glazunov, J. Carlsson, and A. Majidzadeh, "Evaluation of a Simplified Random-LOS Measurement Setup for Characterizing Antennas on Cars", in *2017 11th European Conference on Antennas and Propagation (EuCAP)*, 19–24 March 2017, Paris, France.

[i] A.A. Glazunov, **M.S. Kildal**, and J. Carlsson, "Impact of Azimuthal Antenna Pattern Sampling and Variation on Throughput Measurements", in *2019 6th IEEE International Conference on Antenna Measurements and Applications (CAMA)*, 23–25 October 2019, Bali, Indonesia.

x

Acronyms

5G	fifth generation of wireless communication
AC	anechoic chamber
AoA	angle of arrival
AUT	antenna under test
CATR	compact antenna test range
DL	downlink
DUT	device under test
EIRP	effective isotropic radiated power
EIS	effective isotropic sensitivity
EMC	electromagnetic compatibility
GER	group error rate
LNA	low noise amplifier
LOS	line-of-sight
LTE	long term evolution
MIMO	multiple-input multiple-output
MISO	multiple-input single-output
MoM	method of moments
MPAC	multiprobe anechoic chamber
MRC	maximal-ratio combining
MSE	mean squared error
NF/FF	near-field to far-field
OTA	over-the-air
PA	power amplifier
PEC	perfect electric conductor
PO	physical optics

QAM	quadrature amplitude modulation
QPSK	quadrature phase shift keying
random-LOS	random line-of-sight
RC	reverberation chamber
RF	radio frequency
RIMP	rich isotropic multipath
RMC	reference measurement channels
RSRP	reference signal received power
RX	receiver
SAE	single antenna element
SC	selection combining
SIMO	single-input multiple-output
SISO	single-input single-output
SNR	signal to noise ratio
STD	standard deviation
TBS	transport block size
TIS	total isotropic sensitivity
TPUT	data throughput
TRP	total radiated power
TX	transmitter
UL	uplink
ULA	uniform linear array
UPA	uniform planar array
ZF	zero forcing

Contents

I Introductory Chapters

II   Included Papers

Part I

Introductory Chapters

Chapter 1

Introduction

The continuous development of wireless communications has lead to more connected devices, as well as the exploration of the usage of millimeter-wave bands. Among the increasing amount of devices that use wireless communications there are now vehicles and other devices with large form factor. As a part of the fifth generation of wireless communication (5G) also comes the introduction of millimeter-wave bands, to support the increased demand for higher data rates.

To verify that the wireless devices work as they are intended to, there is the need for reliable, cost-effective and simple testing solutions. There will also be an increased need for over-the-air (OTA) testing, since the antennas will become deeply integrated in those devices and many will lack external connectors, especially at higher frequencies. The technologies that have been used for smaller devices and the current mobile communication frequencies, below 6 GHz, are mainly based on three different technologies, as described in [1]. They consist of the multiprobe anechoic chamber (MPAC), the two-stage method and the reverberation chamber (RC). However, it is not problem-free to adopt these methods, neither for vehicular testing, nor for higher frequencies.

A hypothesis has been stated in [2] as a tool for testing wireless devices under controlled conditions. The hypothesis states that *"If a wireless device is tested with good performance in both pure-LOS and RIMP environments, it will also perform well in real-life environments and situations, in a statistical sense"*. Two edge environments are introduced, random line-of-sight (random-LOS), which is a type of pure line-of-sight (pure-LOS) environment, and rich isotropic multipath (RIMP). These two can be seen as opposites of each other. RIMP is an environment with many scatterers and many incoming signals to the receiver, whereas random-LOS has one dominant contribution. The hypothesis is based on the assumption that a real-life propagation channel would lie somewhere in between these two edges.

1.1 Aim of the Thesis

The aim of the thesis is to investigate the random-LOS OTA environment and its use for testing. Moreover, part of this is to develop a cost-effective measurement system and investigate the limitations and possibilities for testing different passive and active devices. The study has been divided into three main parts.

The first part focuses on how a random-LOS measurement setup can be realized for vehicular applications below 6 GHz and for smaller devices at the 28 GHz band. Two different types of realizations are presented, a dual-polarized virtual planar array antenna, as well as two parabolic cylindrical reflectors with dual-polarized linear array feeds. The thesis presents how the last two setups were manufactured using molded fiberglass and extruded aluminum profiles.

The second part focuses on numerical and experimental verification of the manufactured systems. The numerical verification is performed using a Matlab implemented physical optics (PO) code, which was developed at the Antenna group at Chalmers, as well as a method of moments (MoM) software, WSAP, implemented in C++ [3]. The numerical results have been verified with measurements using the presented systems. The verification has mainly been based on power and phase variations, within different test zones. The results have been studied for different test zone sizes placed at different distances from the system.

The third part focuses on how the system can be used in order to perform passive and active measurements. The measurement procedures have been described in detail in this part. Results are also presented for both passive antenna measurements, as well as for active 2×2 multiple-input multiple-output (MIMO) measurements for a complete vehicle.

1.2 Thesis Outline

The thesis is divided in two parts, the first contains six chapters to introduce the reader to the research topic and presents the main aspects of the work. The second part includes the Author's most relevant contributions to the research area in terms of appended papers. Additional non-appended publications by the Author can be found in the Section *"List of Publications"*.

The first part of the thesis contains the following chapters. Chapter 1 gives a short introduction to the area and states the aim of the thesis, as well as the contributions of the Author. Chapter 2 provides the background, for better understanding of the following chapters. This includes an introduction of wireless communication and various OTA measurement techniques, both for passive antennas and active devices. The real-life hypothesis is also introduced together with a detailed description of the two edge-environments, RIMP and random-LOS. In Chapter 3, three different random-LOS setups are described, the first consisting of a virtual planar array

antenna and the second two of a cylindrical reflector antenna with a dual-polarized linear feed array. Chapter 4 presents the numerical and experimental characterization of the test zone of the systems. In Chapter 5, passive and active measurements with the systems are presented. Chapter 6 gives a summary of the main contributions and describes different future work directions.

Part of the notation and figures in the first part of the thesis have been modified, compared to the appended papers, in order to homogenize the introduction.

1.3 Contributions of the Author

In this section the contributions of the Author are stated for all of the appended papers.

- **Paper [A]:** The Author is the main contributor to this paper. The Author has done the simulations using the software in [3], performed the measurements, post-processed the measurement data as well as written the paper.

- **Paper [B]:** The Author is the main contributor to this paper. The Author has continued the work of the third author and performed the simulations using the PO code that the third author originally wrote. The feed array antenna was previously designed in paper [4] by the second author. The Author has performed the measurements, post-processed the measurement data as well as written the paper.

- **Paper [C]:** The Author is the main contributor to this paper. The Author has performed the full system simulations, the system measurements, the post-processing of the measurement data as well as written the majority of the paper. The design of the feed array antenna, including the array measurements and the parts in the paper related to the feed array, which was performed by the second author of the paper.

- **Paper [D]:** The Author is the main contributor to this paper. The Author has done the simulations using the software in [3], post-processed the simulation data as well as written the paper.

- **Paper [E]:** The Author is the main contributor to this paper. The Author has done the simulations, using the PO code that the second author originally wrote, post-processed the simulation data as well as written the paper.

Chapter 2

Background

This chapter introduces the reader to the topics and background information relevant to the rest of the thesis. First, a brief overview of wireless communication theory and principles is given together with a classification of measurement techniques for passive and active devices. Finally, the real-life hypothesis [2] and the relevant two edge environments are introduced: the RIMP and random-LOS.

2.1 Wireless Communication

In order to understand the behavior of wireless devices, we need to consider the basic background of wireless systems. The wireless channel represents the path of a signal as it travels from the transmitter (TX) to the receiver (RX). The signal can take multiple different paths, which is commonly referred to as multipath [5]. These paths arise when the radiated energy from the TX is reflected, scattered, or diffracted by different objects in the surrounding environment. A direct path between the TX and the RX is called line-of-sight (LOS).

In a free-space environment the radiated power will propagate according to Friis transmission formula [6]. The formula is usually expressed as the ratio between the received power, P_r, and transmitted power, P_t, according to

$$\frac{P_r}{P_t} = \left(\frac{\lambda}{4\pi d} \right)^2 G_t G_r, \tag{2.1}$$

where λ is the wavelength, d is the distance between the TX and RX, G_t and G_r are the TX and RX antenna gain, respectively [7]. Friis transmission formula is applicable when the TX and RX are in the far-field of each other. This means that the antennas have to be separated with a distance

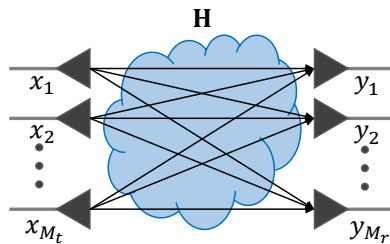$$d > \frac{2D^2}{\lambda} , \tag{2.2}$$

Figure 2.1: Illustration of a MIMO system.

where D is the largest linear dimension of either of the two antennas [7].

The signal received by the RX varies in time, as the RX or TX is moving or as the surrounding environment is changing. In a multipath environment this variation arises from the constructive and destructive summation of the received signals coming from different paths, with different lengths and therefore different phases. This variation is known as fading [5]. Fading can be divided into slow and fast. Slow fading refers to slower fluctuations over a longer period of time, e.g., due to shadowing from a building. Fast fading refers to faster fluctuations over a shorter period of time, e.g., scattering from surrounding objects. Fading that varies over time, due to the movement of the TX/RX or objects in the surrounding, will give rise to a Doppler spread. Moreover, in a multipath environment, the transmitted signal will take different paths with different lengths, which will result in a time spread of the received signal. This spread is called delay spread. Since the signal will take different paths, it will also give rise to a spread in the angle of arrival (AoA) of the different multipath components.

The need for higher reliability and increased performance for wireless devices has led to the use of multiple antennas on both the TX and the RX sides, see Fig. 2.1. The number of TX and RX antennas are denoted M_t and M_r, respectively. Depending if a single or multiple antennas are used at the TX and RX, the systems are denoted as single-input single-output (SISO), single-input multiple-output (SIMO), multiple-input single-output (MISO) and multiple-input multiple-output (MIMO) scenarios [8]. Input refers to the TX side and output refers to the RX side and single and multiple refers to how many antennas that are used.

A MIMO system can be mathematically described by

$$\mathbf{y} = \mathbf{Hx} + \mathbf{n} \, , \tag{2.3}$$

where $\mathbf{y} \in \mathbb{C}^{M_r \times 1}$ and $\mathbf{x} \in \mathbb{C}^{M_t \times 1}$ are the channel output and input, respectively [9]. $\mathbf{H} \in \mathbb{C}^{M_r \times M_t}$ is the channel matrix and $\mathbf{n} \in \mathbb{C}^{M_r \times 1}$ is the noise vector. It is possible to decompose the MIMO channel into independent parallel channels. More independent channels can be achieved in a more rich scattering or multipath environment than in a LOS environment [10]. However, the number of independent channels, R, is limited by $R \leq \min(M_t, M_r)$, and in general, by the rank of the channel matrix $\mathbf{H}$.

The stability of the wireless system can be increased by using independent channels to transmit or receive several copies of the same data, this is referred as diversity. By using diversity, the system becomes less vulnerable to fading dips, and thereby also more stable. There exist different schemes to combine the data at the receiver ports, e.g., selection combining (SC) or maximal-ratio combining (MRC) [8]. In SC, the strongest signal is selected, whereas in MRC, the received signals at all the ports are weighted and summed together to obtain the maximum signal to noise ratio (SNR). In MRC, the weights are chosen proportionally to the SNR at the ports.

Instead of providing diversity, the multiple antennas can be used for multiplexing. In multiplexing, different data will be transmitted on every channel, increasing the capacity of the MIMO system. In order to separate the signals, different schemes can be used, e.g., singular value decomposition or zero forcing (ZF). In this thesis, we have used a ZF receiver, which decouples the matrix channel into M_t parallel scalar channels with additive noise [5]. The SNR of the i-th data stream using ZF is given by

$$\gamma_i^{\text{ZF}} = \frac{\gamma_t}{M_t[(\mathbf{H}^H\mathbf{H})^{-1}]_{i,i}} \ , \tag{2.4}$$

where γ_t is the transmit SNR, the superscript ^{H} is the conjugate transpose and $[\mathbf{X}]_{i,i}$ denotes the i-th diagonal entry of the matrix $\mathbf{X}$ [5]. Assuming unit variance noise, the SNR expression in Eq. (2.4) can be directly converted to power.

The threshold receiver model, presented in [11], can be used to calculate the data throughput (TPUT) from the received power. It has been noted that in a static environment, the group error rate (GER) changes quickly from 100% to 0% when the power P reaches a certain threshold power, P_t. This can be written as

$$\text{GER}_{\text{ideal}}(P) = \left\{ \begin{array}{ll} 1, & \text{when } P < P_t \\ 0, & \text{when } P > P_t \end{array} \right. . \tag{2.5}$$

The TPUT can then be straightforwardly expressed in terms of the maximum TPUT, TPUT_{max} and the GER,

$$\text{TPUT} = \text{TPUT}_{\text{max}} * (1 - \text{GER}(P)) \ . \tag{2.6}$$

The value of TPUT_{max} depends on parameters such as modulation and coding.

Fig. 2.2 shows the threshold levels measured for different orientations of a device under test (DUT) in a static environment. It can be seen that the TPUT abruptly changes from full to zero and behaves in the same way as a conducted measurement, i.e., a step-like curve. This transition happens at different power levels. For example, with the orientation, due to the non-isotropic radiation pattern of the DUT. These threshold values are what we are interested in measuring in the random-LOS measurement setup. Since the change is very steep, it is possible to represent the threshold by the power level at which it occurs, as shown with a star ($*$) in the figure.
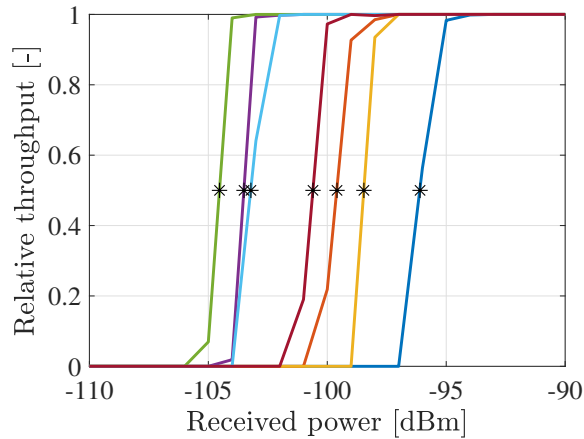
Figure 2.2: Examples of threshold levels for different orientations of a DUT in a static environment.

2.2 Over-the-Air Characterization of Antennas and Devices

The measurement task has the critical role of verification and certification of the performance of the antenna, as well as to guide its design. This is true for standalone antennas and even more so for antennas integrated in active devices. While the former can be treated with well-established passive measurement techniques the latter poses additional challenges. Since direct access to the antenna ports within an active device is often challenging and sometimes unrealistic, OTA measurement techniques must be adopted to perform air-borne and device-level performance evaluation.

2.2.1 Passive Measurements

In order to characterize antennas, several relevant properties are of interest. Some of the more traditional passive antenna properties that can be measured are, for example, the far-field radiation pattern in principal planes, the antenna directivity, gain, beamwidth, as well as the radiation efficiency [7, 12]. The reflection coefficient and mutual coupling are also important properties; however, these can be measured using only a cabled setup. The importance of each property and their desired values is application dependent. Most of the mentioned properties have been originally defined for situations where both the transmitting and receiving antennas are fixed in space.

Antennas are traditionally characterized in free-space environments, in the far-field of the antenna under test (AUT), Eq. (2.2). This scenario describes the behavior of the AUT in isolation and not in its immediate proximity. To reproduce a free-space environment an anechoic chamber (AC) can be used to suppress all reflections. An AC
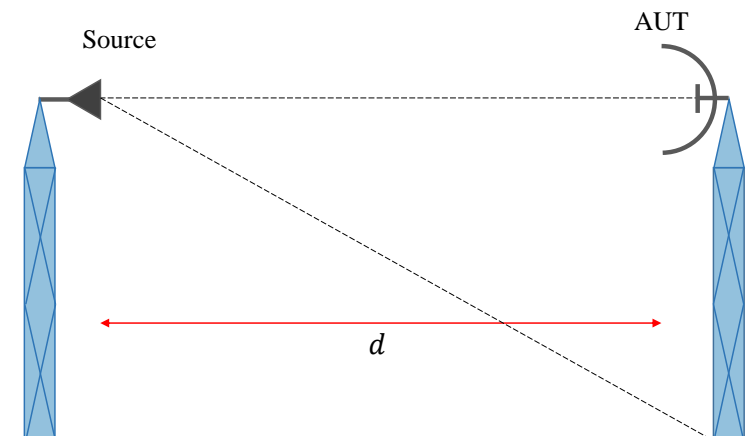
Figure 2.3: Elevated free-space range.

has walls, floor and ceiling covered in radio frequency (RF)-absorbing materials [13]. The far-field condition requires to illuminate the AUT with a plane wave, i.e., with uniform amplitude and phase. This is an ideal condition, but can be practically achieved with different setups, such as far-field ranges, compact antenna test range (CATR) and near-field to far-field (NF/FF) methods [14, 15].

Far-field Range

The far-field range, as the name implies, measures directly in the far-field of the antenna. This can be achieved by separating the source antenna and the AUT with a distance d according to Eq. (2.2). As an example, for a large antenna with the largest dimension $D = 1.5\,\text{m}$ at the frequency $f = 2\,\text{GHz}$, the separation distance becomes $d = 30\,\text{m}$. Instead, at $28\,\text{GHz}$ a distance of $d = 17\,\text{m}$ is required for an antenna with $D = 0.3\,\text{m}$. As a result, for electrically large antennas, where the size is large in terms of the wavelength, a large separation distance is needed. Due to these potentially large distances, it is common to realize the far-field ranges outdoor. In outdoor environments, problems related to reflections from the ground, surrounding objects, as well as weather conditions come into play. For very large objects in terms of wavelengths, the minimum separation distance can become too large even for outdoor ranges, and therefore other methods are required.

Two examples of outdoor far-field ranges are the elevated and the slant ranges [7]. A schematic drawing of an elevated free-space range is shown in Fig. 2.3. The elevated free-space range is designed such that the source antenna and AUT are mounted on two towers opposite each other at the same height. The tower height should be sufficient to reduce unwanted ground reflections, which can affect the measurement results. To improve this aspect, the first null of the radiation pattern of the source antenna is directed towards the base of the AUT tower [15]. The slant free-space

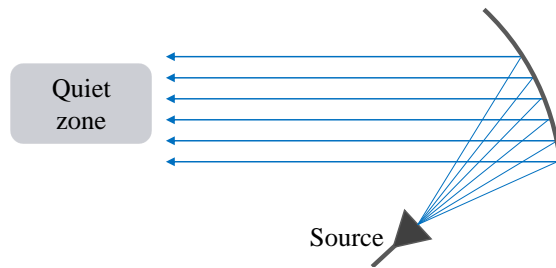Figure 2.4: Compact antenna test range.

range is more compact than the elevated free-space range, and makes use of only one tower. The AUT is mounted on the tower and the source antenna is instead placed on the ground. The source antenna is oriented such that the maximum radiation pattern point is directed towards the center of the AUT and the first null in the pattern is directed towards the base of the AUT-tower.

Compact Antenna Test Range

Another option for creating a far-field condition for the AUT is to use a CATR. The CATR, as the name implies, is a more compact measurement range compared to the far-field ranges. It makes use of a reflector antenna to create a plane wave at the location where the AUT is to be placed [16]. This solution enables smaller indoor ranges that can be used for measuring radiation patterns with high accuracy.

In a CATR, a reflector is illuminated by an offset feed antenna [7]. The diverging rays from the feed antenna are collimated by the reflector, and nearly planar wavefronts will be generated in a limited volume in front of the reflector, see Fig. 2.4. This volume is called the test or quiet zone, and must contain the AUT. In the quiet zone, the amplitude and phase variations are small, typically with a peak-to-peak variation of $\pm 5°$ in phase and of $\pm 0.5\,\mathrm{dB}$ in amplitude [14].

A common way to realize a CATR is by using a paraboloidal reflector with a point feed, or alternatively, a parabolic cylindrical reflector with a line feed [16]. The reflector can generally operate over a large frequency band, where the lower frequency limit is determined by diffraction from the edges of the reflector, whereas the upper frequency limit is determined by the imperfections of the surface [17]. However, the system is also limited by the bandwidth of the feed antenna. In general, it is easier to design a point feed with a wider bandwidth, compared to a line feed; however, the shape of the cylindrical reflector is simpler.

There exist different sources for imperfections in the plane field generated by the CATR. The source feed can block the aperture, which can be solved by offsetting the feed relative to the reflector. The feed can radiate directly into the quiet zone, which can be reduced by using absorbing materials. Diffraction from the edges of the reflector will also reduce the performance of the system. The resulting constructive

and destructive interferences are often the main source of the amplitude and phase ripple in the quiet zone [7]. The edge diffraction can be improved by for example serrated or rolled edges [18]. Another option can be to reduce the edge illumination by adjusting the radiation pattern of the feed to drop off towards the edges.

Near-field to Far-field Method

The radiation characteristics of the antenna changes with the distance, and progressively converge to the far-field radiation pattern. By using an NF/FF transformation method, it is possible to sample the near-field radiation of the AUT and convert it to the far-field characteristics by using Fourier transformation [7, 19]. The samples are collected in complex form, including both amplitude and phase information, by measuring on a well defined grid. The grid takes normally one of the following shapes: a plane, a cylinder or a sphere in front of or around the AUT. The spherical grid is the most complete, but also the most cumbersome one, in terms of computational time, positioning and equipment [7].

Measurements over a spherical grid can be performed by either fixing the probe antenna and rotating the AUT, or fixing the AUT and rotating the probe around it [20]. Since all sampled near-field data has to be post-processed with numerical integration and Fourier transformation, no real-time or dynamic data can be acquired by using an NF/FF transformation measurement method.

2.2.2 Active Measurements

The introduction of active devices and the increased integration of antennas and electronics create the need for testing the performance of the complete wireless device. The testing must then be performed on the system level, including the antenna/antennas, the modem, and the device as a whole. In order to avoid the influence of connected cables and the progressive disappearance of connectors, it is natural to perform these measurements OTA. Common tests for evaluating the radiated performance of active devices are through the measurements of total radiated power (TRP) in the uplink, total isotropic sensitivity (TIS) and data throughput (TPUT) in the downlink [1, 21, 22]. TPUT is often used as the MIMO metric to distinguish between good and bad devices. The effective isotropic radiated power (EIRP) is another measure which incorporates both the gain and the transmitted power [22]. TRP can be calculated by performing an integration over the whole sphere. The effective isotropic sensitivity (EIS) value, instead, gives a measure of the sensitivity of the system. In [23] it is described how one can perform EIRP and EIS measurements of base stations using a spectrum analyzer and signal generator, respectively. The EIRP and EIS can be measured in, e.g., indoor far-field ranges, CATR and NF/FF [23].
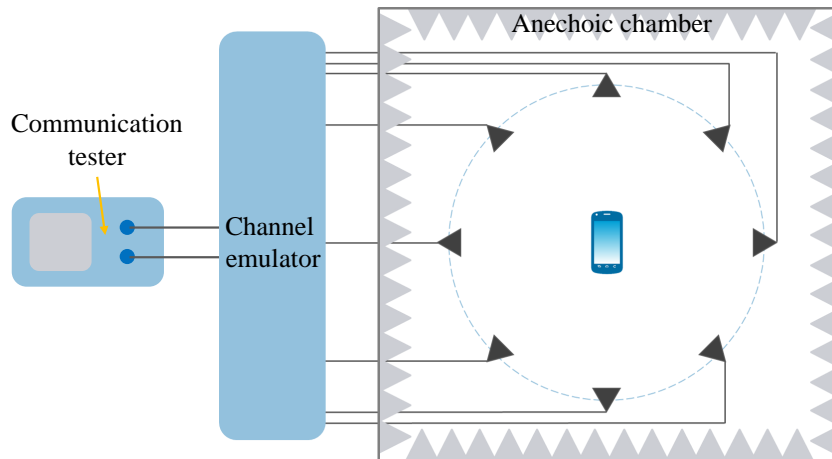
Figure 2.5: The multiprobe anechoic chamber setup.

There are different methods used to test the performance of active devices, such as mobile phones, tablets, and laptops, but also larger devices such as vehicles. Among these, the most common ones are the MPAC, the two-stage method and the RC. In this section, these methods are presented in the context of general MIMO measurements.

Multiprobe Anechoic Chamber (MPAC)

In the MPAC, a set of probes is positioned around the DUT inside an AC, see Fig. 2.5. The probes are usually placed in a 2D ring or 3D sphere, but can also be positioned in clusters [1]. The measurements are performed by making use of a communication tester or base station simulator, which is connected through a channel emulator to the probes. Different propagation and fading environments within the test zone can be realized with the channel emulator by synthesizing different channel models [24, 25]. The probes are individually fed, and by changing their amplitude, phase and delay as well as making use of their different locations to introduce an angular spread, different channel models can be realized.

The number of probes that are needed depends on the number of fading channels (one for each probe), the DUT size, and polarizations [1]. With the goal of reducing the number of probes needed in the setup, some probe selection algorithms for the 3D case are presented in [26]. The DUT size is important since the AC needs to be large enough for the DUT and probes to be in the far-field of each other. As a minimum amount, eight probes with a spacing of 45° are used for the ring solution, and at least three clusters must be used for the clustered version [1]. Twice the number of probes are needed if dual polarization is desired. Moreover, the channel emulator needs a sufficient number of ports to support the probes that are used in the setup, which makes the cost of the system quickly increase with the number of probes [27]. As a
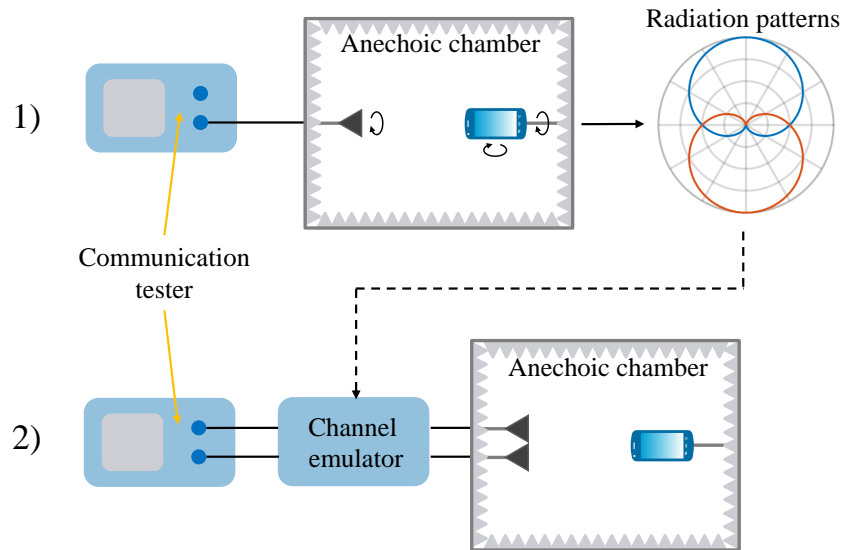
Figure 2.6: The two-stage method. The first stage shows how the radiation patterns are obtained and the second stage shows how the channel model is applied to the radiation patterns and fed to the DUT. The feeding to the DUT can be performed either through a conducted or radiated connection, where the latter is shown in the figure.

reference, a multiprobe setup for cars has been studied in [28].

Two-stage Method

The two-stage method requires, as the name implies, the execution of two subsequent measurement steps, see Fig. 2.6. First, the complex antenna radiation patterns of the DUT are accurately measured. Second, the channel model is applied to the radiation patterns in a channel emulator, and the resulting signal is fed to the DUT to emulate the desired communication link [1].

The radiation patterns, in the first stage, can be obtained by simulations or by measurements [29]. As discussed earlier, traditionally passive measurements are performed by connecting a cable to the device; however this might affect the results or might not be feasible. An alternative way to acquire the radiation patterns are by a built-in testing mode in the device, which would report relative phase and amplitude of the internal receiver [1,30]. However, it requires this additional functionality to be present in the DUT. The commonly built-in reference signal received power (RSRP) measurement provides power measurements but no phase information. If the built-in test mode for relative phase and amplitude is available, the incoming signal can be calibrated, and it is then possible to obtain the complex radiation patterns. In this configuration, measurements are performed inside an AC with a communication tester [29].

In the second stage, the output of a communication tester is connected to the

input of a channel emulator. In the channel emulator, the desired channel model is applied to the radiation pattern data, which was acquired in the previous stage. In the last part of the second stage, the connection between the channel emulator and the DUT can be achieved either through a conducted or radiated mode [1]. In the conducted mode, RF-cables are connected between the channel emulator and the internal antenna ports on the DUT. However, in the absence of internal antenna ports or to include the self-interference of the DUT, the radiated mode can be adopted [31]. In this configuration, the transfer matrix between the channel emulator and the DUT is measured, and its inverse is applied to the transmit signal. This allows to calibrate the system and make the received signals be the intended signal from the channel emulator [1]. A specific version of the radiated two-stage method is called the wireless cable method, where the step of measuring the transfer matrix is avoided [32]. Instead the RSRP values from the DUT are used to determine complex weights applied in the channel emulator, in order to achieve a wireless cable setup.

The radiated two stage method also makes use of a channel emulator, as in the MPAC setup, however here fewer probes are needed in order to perform the measurements. The number of probes and interface channels in the channel emulator is equal to the number of ports on the DUT [32]. This method could potentially be used for evaluating antenna systems on vehicles or other large devices [32,33]. Since the radiation characteristics of the DUT are acquired in the first step of the two-stage method, it might be hard to account for adaptive DUT patterns [32].

Reverberation Chamber (RC)

The RC, in opposite to an AC with its absorbing walls, consists of a metal cavity that supports a large number of modes at the operating frequency [34]. Traditionally, the RC has been used for electromagnetic compatibility (EMC) testing [35,36]. The chamber contains metal plates, so-called mode stirrers, that are moved inside the chamber to excite different modes, see Fig. 2.7. In front of the chamber antennas inside the RC, a metal shield is placed to avoid a LOS component. The DUT is placed on a turntable, and the polarization is changed by switching between different chamber antennas. In this way, many independent samples can be collected, and the accuracy can be improved [37]. The RC emulates a RIMP environment, which will be described more in detail in Section 2.3.1. Statistically, the emulated environment can be described as a multipath Rayleigh fading environment.

In order to perform a measurement in an RC, the setup needs to be calibrated. In the calibration step, the average power transfer function of the chamber, which is proportional to the radiation efficiencies of the transmitting and receiving antennas, is measured [38]. The active measurements are performed by connecting a communication tester to the chamber antennas in the RC. The RC provides a natural Rayleigh fading environment and, while less flexible, it does not need a channel emulator to synthesize it. However, a channel emulator can be used if additional variations in,
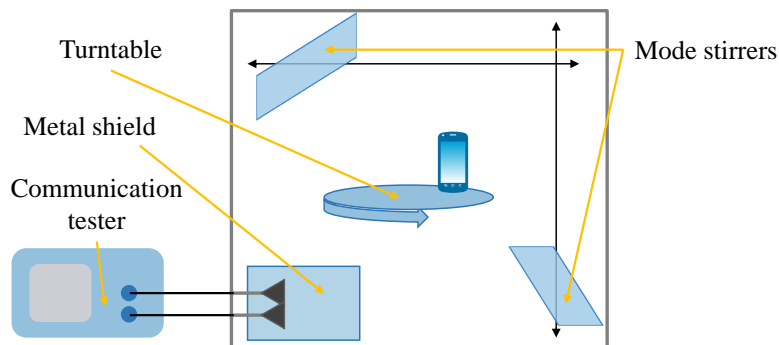
Figure 2.7: The reverberation chamber.

e.g., Doppler and delay spread are desired [39]. There exists no specific test zone inside the chamber, but the DUT should be placed at least $\lambda/2$ away from any metal wall/plate [34]. Due to this, the RC can also be used to test large form factor devices, where a large form factor is defined as when one of the physical dimensions of the device is larger than 42 cm [40].

2.3 Real-life Hypothesis

As described in this chapter, there exist different ways to evaluate the active performance of wireless devices. They all have their advantages and disadvantages and are suited for different types of devices and user environments. The methods that have been mentioned in the previous sections are based on different models of real-life environments. Those that rely on channel emulators and channel models to reproduce different scenarios offer greater flexibility, but can be cumbersome and expensive [27]. On the other hand, performing real-life tests is not a solution, due to the cost, time and poor repeatability of an uncontrolled environment. Ideally, the objective is to verify that the DUT works well in all real-life environments in which it will be used. However, this would not be feasible, and a compromise needs to be found.

An alternative approach is presented in [2], where a hypothesis is stated as follows "*If a wireless device is tested with good performance in both pure-LOS and RIMP environments, it will also perform well in real-life environments and situations, in a statistical sense*". This hypothesis still stands to be proven, but it offers an appealing and practical framework for evaluating different devices in a cost and time-effective way. A more detailed description of the two edge environments, RIMP and pure LOS, expressed as random-LOS, is presented in Fig. 2.8 and in the following sections. Depending on the use case and operating frequency, one of these two environments might be more important or relevant than the other.

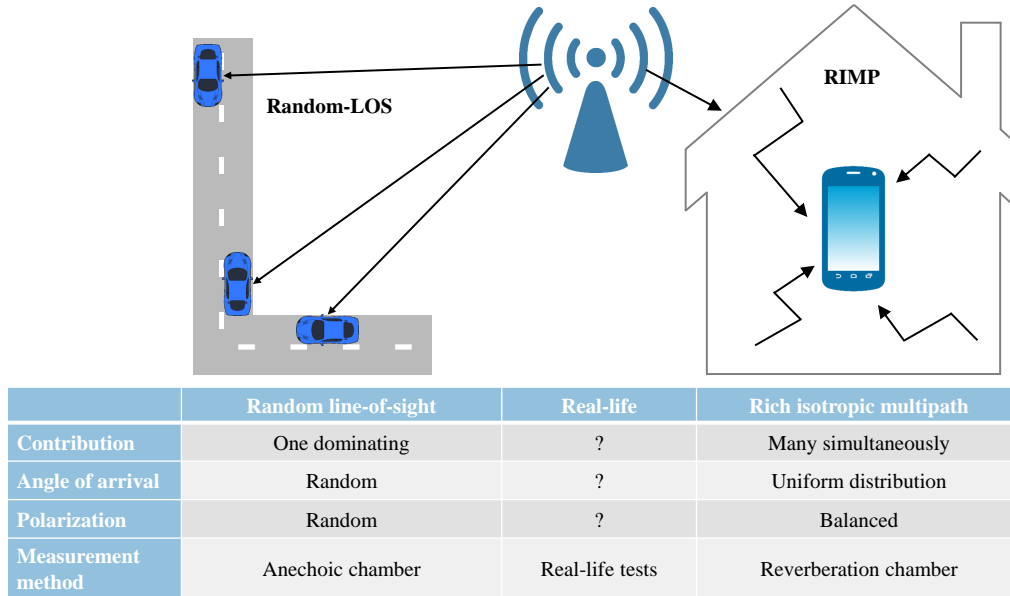|	Random line-of-sight	Real-life	Rich isotropic multipath
Contribution	One dominating	?	Many simultaneously
Angle of arrival	Random	?	Uniform distribution
Polarization	Random	?	Balanced
Measurement method	Anechoic chamber	Real-life tests	Reverberation chamber

Figure 2.8: Comparison between random-LOS and RIMP. The random-LOS case is represented by a highway scenario with cars. The RIMP case is represented by an indoor environment with a lot of scatterers and no LOS to the base station.

2.3.1 Rich Isotropic Multipath

The RIMP environment is an ideal fading environment, which despite not existing in reality, has proved to be very useful [34]. The abbreviation RIMP is made by the following words. The first word, *rich*, implies that there are many incoming waves to the receiver simultaneously. *Isotropic* refers to that the AoA of the incoming waves are on average uniformly distributed over the unit sphere, and thus the orientation of the DUT will not matter. The last word *multipath* means that the waves have taken multiple paths to the receiver. All these characteristics can be emulated together in an RC. The amplitude variation of the received signals by the DUT will follow a Rayleigh distribution, while the phase is uniformly distributed [34, 41].

As summarized in the table in Fig. 2.8, the RIMP environment is characterized by many simultaneously incoming waves, a uniform distribution of the AoA, and a polarization balance. This can be similar to, e.g., an indoor environment for mobile phones operating at the typical sub-6 GHz bands. A real environment is normally not isotropic; however, if a device is used with arbitrary orientation, statistically this would become the case [34]. User devices, such as mobile phones, are typically used in different orientations, e.g., surf mode and talk modes. An initial study of smart phone orientation in real environments has been studied in [42].
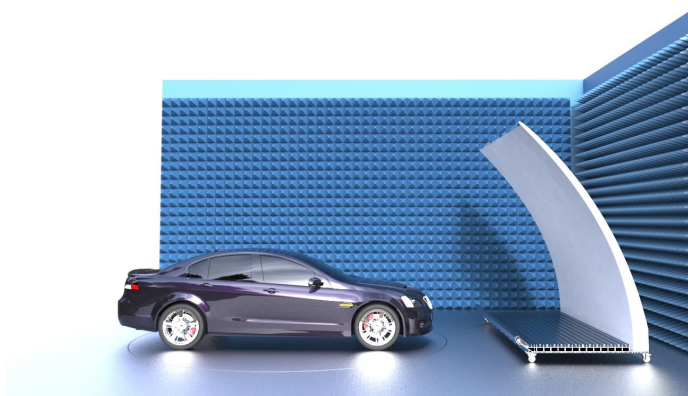
Figure 2.9: Illustration of the random-LOS measurement setup solution with a reflector and a linear array feed for creating a plane wave illumination of the car.

2.3.2 Random Line-of-Sight

In opposite to RIMP, the random-LOS environment has only one dominant contribution. This consist of maximum two orthogonal polarizations, with independent amplitude and phase, coming from the same direction. Most of the time this is a LOS component, but can also be a strong diffracted or scattered wave [43]. Unlike the traditional LOS, in a random-LOS environment at least one of either the transmitter or receiver is randomly oriented. Usually, this is the user device, since the base station normally is placed in a fix position [44]. By considering an ensemble of users over time, the statistics of the DUT orientation will become increasingly random, and thereby the randomness in the LOS component will increase.

As summarized in the table in Fig. 2.8, for random-LOS, both the AoA and the polarization can be modeled as random variables. For a randomly oriented handset device (e.g., a mobile phone or tablet), both the polarization (considering linear polarization) and the AoA of the incoming wave will change relative to the DUT. A handset device would typically be oriented in any direction in space, and would therefore experience a 3D random-LOS environment. This has been studied more in detail in terms of polarization-MIMO in [10]. Vehicles, instead usually move on a 2D plane, with some slight elevation angles. As a result they mainly experience an AoA in 2D, i.e., a 2D random-LOS environment. This corresponds well to an open area environment with a LOS to the base station, e.g., a typical highway. An idea for realizing a random-LOS test environment for testing the wireless performance of vehicles was presented in [45, 46]. This idea was further developed in [47] using a parabolic cylindrical reflector, similar to a CATR, see Fig. 2.9. The aim of the system is to provide a cost-effective and simple solution for testing the performance of antennas and active devices on vehicles or other large devices. Additional work on different aspects of random-LOS can be found in [4, 48–50] and [b]-[i].

17

3

Realizations of the Random-LOS Measurement System

The random-LOS measurement system can be realized in different ways. The main goal is to generate a plane wave to emulate the far-field condition. Two solutions to reproduce this are a planar array and a parabolic cylindrical reflector with a linear feed array. In this chapter, three dual-polarized systems will be introduced, one virtual planar array and two cylindrical reflectors with linear feed arrays, operating at different frequencies.

3.1   Virtual Planar Array Antenna

A plane wave can be realized by using a planar array [20, 51, 52]. In [49], simulations of a planar array for random-LOS testing are presented. The array antenna intended for the random-LOS measurement system is a 2D array antenna, shown in Fig. 3.1. The array contains $N = N_v \times N_h$ antenna elements, where N_v and N_h are the numbers of elements in the vertical and the horizontal direction, respectively. By increasing the number of elements, a larger test zone can be achieved. Enlarging the array in the vertical and the horizontal direction, will give a larger test zone height and width, respectively. The uniform planar array (UPA) introduced in [A] consists of $N = 8 \times 23 = 184$ antenna elements. However, since that would have been considerably expensive to manufacture, the concept was tested using a virtual UPA. A vertical 8×1 uniform linear array (ULA) was thus moved to different horizontal positions to synthesize the UPA. In the same paper, the UPA performance was compared to the performance of a virtual 1×24 horizontal ULA and a single antenna element (SAE).

The linear 8×1 array in [A] consists of dual-polarized bowtie antenna elements, combined using a distribution network of power splitters and cables, as described in detail in [4]. The element spacing in the bowtie array was $0.11\,\mathrm{m}$, corresponding to
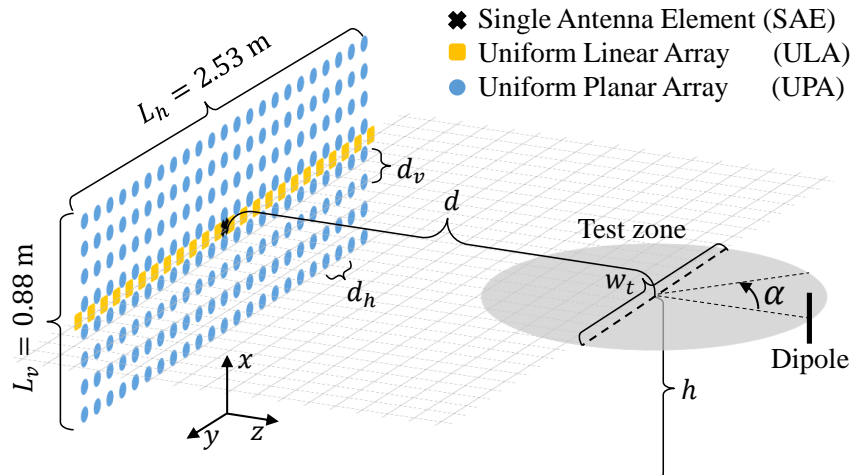
Figure 3.1: Simulation setup for the UPA, the horizontal ULA as well as the SAE. The values for L_h and L_v are given for the UPA.

one wavelength at $2.7\,\text{GHz}$. The bowtie antenna array is surrounded by corrugations on two of the four sides. The system was verified for the $2.7\,\text{GHz}$ band, which is the upper frequency limit for the designed bowtie antenna array.

The planar array performance can be improved by implementing amplitude tapering of the edge elements of the planar array, as described in [D]. In paper [D], a 24×24 element array with amplitude tapering along the horizontal direction was presented. However, in a planar array, it is also possible to perform amplitude tapering of the elements in the vertical direction. In the example presented in paper [D], tapering was applied on the horizontal outermost $50\,\%$ of the elements in the array.

3.2 Reflector Antenna

A reflector antenna system for random-LOS was introduced in [47, 50]. The reflector antenna system consists of a parabolic cylindrical reflector, corrugations and a dual-polarized linear feed array. The linear feed array is located in the focal line of the cylindrical reflector, and corrugations are introduced between the base of the reflector and the feed array.

The metal corrugations realize a soft surface [34, Chapter 8], and for air-filled corrugations, see Fig. 3.2, the corrugation depth d_c should fulfill

$$\lambda/4 < d_c < \lambda/2 \ . \tag{3.1}$$

However, in practice, the depth can be smaller than $\lambda/4$ and a soft boundary condition will still be achieved [34, Chapter 8]. The corrugation periodicity, p_c, should be less than $\lambda/2$ and preferably less than $\lambda/4$. The corrugations in the reflector antenna system are added on both longitudinal sides of the feed array. The corrugations
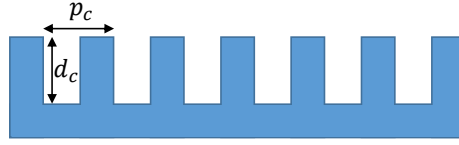
Figure 3.2: Corrugated surface with the corrugation depth d_c and periodicity p_c.
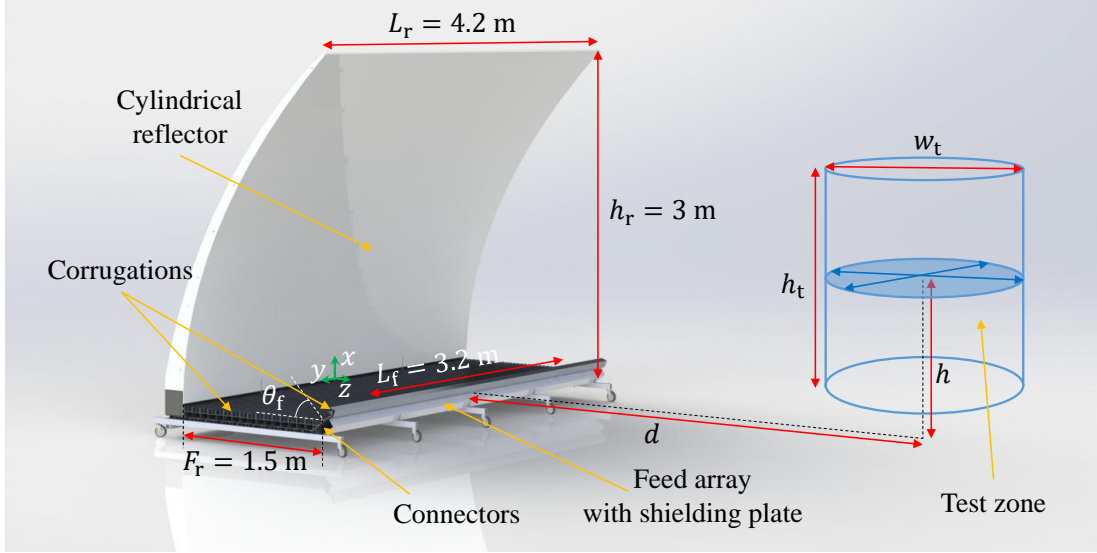
Figure 3.3: Illustration of the cylindrical reflector with the dual-polarized linear array feed of bowtie antennas in the sub-6 GHz system and the cylindrical test zone in front.

between the feed array and the reflector are added to give the same boundary condition for both polarizations, in contrast to a perfect electric conductor (PEC) ground plane. The corrugations on the other side of the feed array are added to reduce the back illumination from the feed into the test zone.

Two systems, designed for two different application areas and frequencies, are shown in Fig. 3.3 and Fig. 3.4. The sub-6 GHz system in Fig. 3.3 is designed to work for frequencies in the range 0.75–6 GHz and gives a large test zone where antennas with large form factor can be tested, such as vehicular mounted antennas. The smaller system shown in Fig. 3.4 is designed for smaller devices in the 28 GHz band.

The cylindrical reflector in both the systems has a profile described by the formula $z(x, y) = x^2/(4F_r)$, where F_r is the focal depth of the reflector. For both systems, the design is such that the feed array can be exchanged to another covering a different frequency range. In this way the system is modular and upgradable.

The feed arrays of the systems are placed along the focal line of the cylindrical reflector and tilted to optimally illuminate the reflector. The feed tilt is $\theta_f = 55°$. All the elements of the feed array are combined using a distribution network to offer two ports, one per polarization.

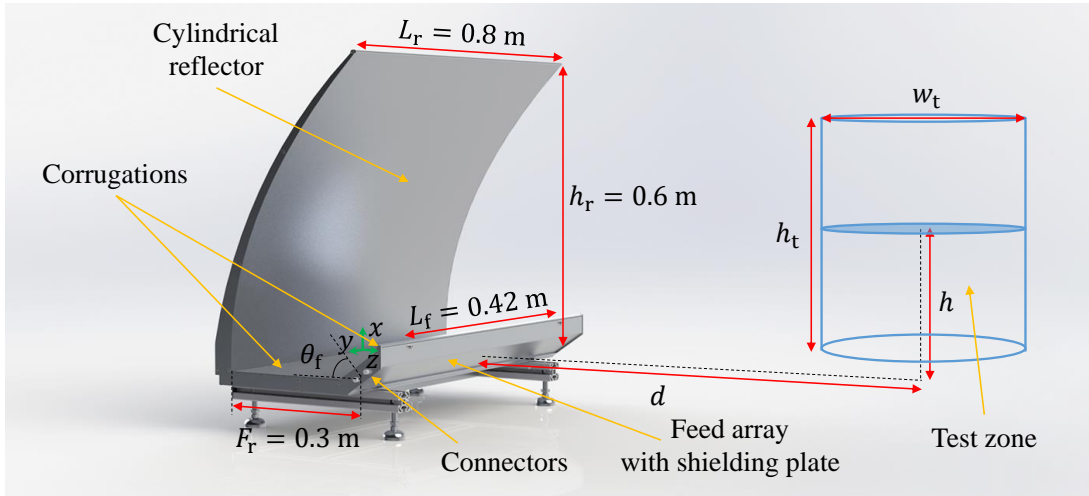Figure 3.4: Illustration of the cylindrical reflector antenna with the feed array tilted in front for the 28 GHz system. The test zone, a cylinder, is shown in front of the reflector antenna.

3.2.1   Sub-6 GHz Reflector

The random-LOS reflector system designed for the sub-6 GHz band is intended for testing devices with large form factor used in open random-LOS environments, such as vehicle mounted antennas. The reflector and feed assembly is 4.2 m wide, 1.8 m deep and 3.3 m high in the outer dimensions. The system is placed on wheels in order to be easily moved in and out of the test chamber or the outdoor open area test site.

The reflector is constructed from four molded fiberglass structures, covered with an aluminum metal sheet on the reflecting side and a thin protective coating. The four structures are mounted next to each other in the horizontal plane, forming the full reflector. This mechanical design makes it possible to widen the reflector, and make the reflector length, L_r, larger. A wider reflector will give a wider test zone, under the assumption that also the feed array is extended. However, the test zone height will not increase, since the height of the reflector remains the same. The seams between the four structures on the reflecting part of the reflector, i.e., the front part of the reflector, are covered with copper foil tape with conductive adhesive. This is done to guarantee the electrical continuity between the separate panels.

This reflector system was initially designed to cover the frequency range 0.75–6 GHz, using three linear feed arrays. The operating frequency of the system is mainly limited by the bandwidth of the feed, as a result other frequencies outside the mentioned band can be measured by employing other feed arrays. The system is initially tested in [B] with a linear feed array covering the 1.5–3 GHz range. This linear feed array consists of 32 dual-polarized bowtie antenna elements, similar to the ones used in the virtual planar array system described in Section 3.1, but with smaller inter-element spacing to cover a larger frequency band without creating grating lobes.

Additionally, two dummy bowtie elements are added to both ends of the array to provide similar embedded element pattern for all elements of the array. The length of the bowtie antenna array is $3.2\,\mathrm{m} + 0.4\,\mathrm{m}$ (active + dummy elements). The array elements are combined using an equal amplitude and phase distribution network of power splitters and cables.

Edge illumination of the reflector gives rise to diffraction that will reduce the accuracy in the test zone. There are different ways to handle this, see Section 2.2.1. In this setup, no edge treatment of the reflector has been performed; however, an attractive alternative has been investigated to reduce the edge illumination from the feed array. This could be done by tapering the feeding of the elements in the feed array.

A feed array improvement using amplitude tapering has been presented in [B]. This was done by adding attenuators with the highest attenuation on the edge elements and lower when closer to the center of the feed array. It should be noted that this type of tapering will only improve the edge diffraction from the sides, but not from the top of the reflector as the array is linear and horizontally aligned.

3.2.2   28 GHz Reflector

The planned frequencies for 5G are 0.41–7.125 GHz and 24.25–52.6 GHz [53]. The higher frequency span is divided in 26.5–29.5 GHz, 24.25–27.5 GHz, 37–40 GHz and 27.5–28.35 GHz bands. The 28 GHz random-LOS measurement system fits well into the last with an operating frequency of 27–28.7 GHz. Thanks to its modularity, the system can be easily adapted to the other bands by swapping the feed array. The 28 GHz system is intended for testing of smaller devices, such as mobile terminals, vehicular antennas and potentially micro-base stations.

A 28 GHz reflector design was introduced in [C]. For the realization, the reflector is divided vertically into three parts. Each of the parts has been manufactured by extruding aluminum profiles, and thereafter mounted together. As a result, two horizontal seams run across the reflector surface. To remove those, and to give a smoother surface than what the aluminum profiles have, a sheet metal plate has been glued to the front of the three profiles. The reflector has a length of $L_r = 0.8\,\mathrm{m}$, a focal depth of $F_r = 0.3\,\mathrm{m}$, and a height of $h_r = 0.6\,\mathrm{m}$.

The feed array elements of the 28 GHz system are multilayer aperture-coupled patch antennas. The linear dual-polarized feed array consists of 64×1 elements, with additional three unexcited elements on each side of the array to reduce the edge effect of nearby elements. The elements are combined with two 64×1 feeding networks, one for each polarization. The feeding network is included in the feed array structure.

It is possible to also improve the performance of the 28 GHz system, by using amplitude tapering of the elements in the feed array. However, this has not been

studied and is left for future work.

Chapter 4

Characterization of the Test Zone

In order to assess the performance of a random-LOS measurement system, the test zone should be characterized. This is described by the field variation in terms of power and phase. First the systems have been simulated with an MoM and a PO algorithm. Details of the implementations are given in Section 4.1. The simulations have then been verified by measurements, as described in Section 4.2. The test zone evaluation, and comparisons between simulations and measurements, are presented in Section 4.3. Finally in Section 4.4, a test zone verification procedure is presented.

4.1 Numerical Simulations

Numerical simulations have been performed for a planar array system at 2.7 GHz, as well as for two reflector systems, one designed for sub-6 GHz and one for 28 GHz. The planar array system is simulated using an MoM code and the reflector systems are simulated with a PO code.

4.1.1 Method of Moments

The field in front of the planar array has been simulated by MoM [3]. The field was computed by making use of reciprocity and superposition principles. In the simulations, a half-wavelength dipole at 2.7 GHz was moved to different points on a grid and its radiation was sampled at the positions of the elements in the planar array, see Fig. 3.1. The sampled field contributions from all the array elements were then superimposed. Due to reciprocity, this is equivalent to the radiated field from a planar array of point sources, where the field is sampled using a half-wave dipole. It should be noted that these simulations only consider isotropic radiation pattern for the elements in the array.

The field variations in front of a UPA were compared to the field variations using a horizontal ULA and an SAE [A]. The setup for these three antenna systems can

Physical Optics Algorithm

1. Define parameters

2. Mesh reflector

Square mesh cells with side length $\lambda/2$

3. Import feed element pattern

4. Loop: feed element j

 i. Interpolate the far-field on the reflector mesh cells
 ii. Calculate the incident field on the reflector, $\boldsymbol{H}_j^{\mathrm{i}}$
 iii. Sum total incident field: $\boldsymbol{H}^{\mathrm{i}} = \boldsymbol{H}^{\mathrm{i}} + \boldsymbol{H}_j^{\mathrm{i}} * tapering$

$\boldsymbol{H}^{\mathrm{i}}$ contains the incident field entries for all the mesh-cells

5. Compute the PO-current, $\boldsymbol{J}$, in the center of each mesh cell

$$\boldsymbol{J} = 2\hat{\boldsymbol{n}} \times \boldsymbol{H}^{\mathrm{i}}$$

6. Multiply $\boldsymbol{J}$ with the cell-area to get the dipole moment

7. Define observation points (the test zone)

8. Loop: Calculate the scattered field $\boldsymbol{E}^{\mathrm{s}}$, at the observation points

Calculate $\boldsymbol{E}^{\mathrm{s}}$ using [34, Sec. 4.2]

9. Calculate the incident field from the feed elements, $\boldsymbol{E}^{\mathrm{i}}$,
at the observation points

10. Get the total field at the observation points: $\boldsymbol{E}^{\mathrm{tot}} = \boldsymbol{E}^{\mathrm{s}} + \boldsymbol{E}^{\mathrm{i}}$
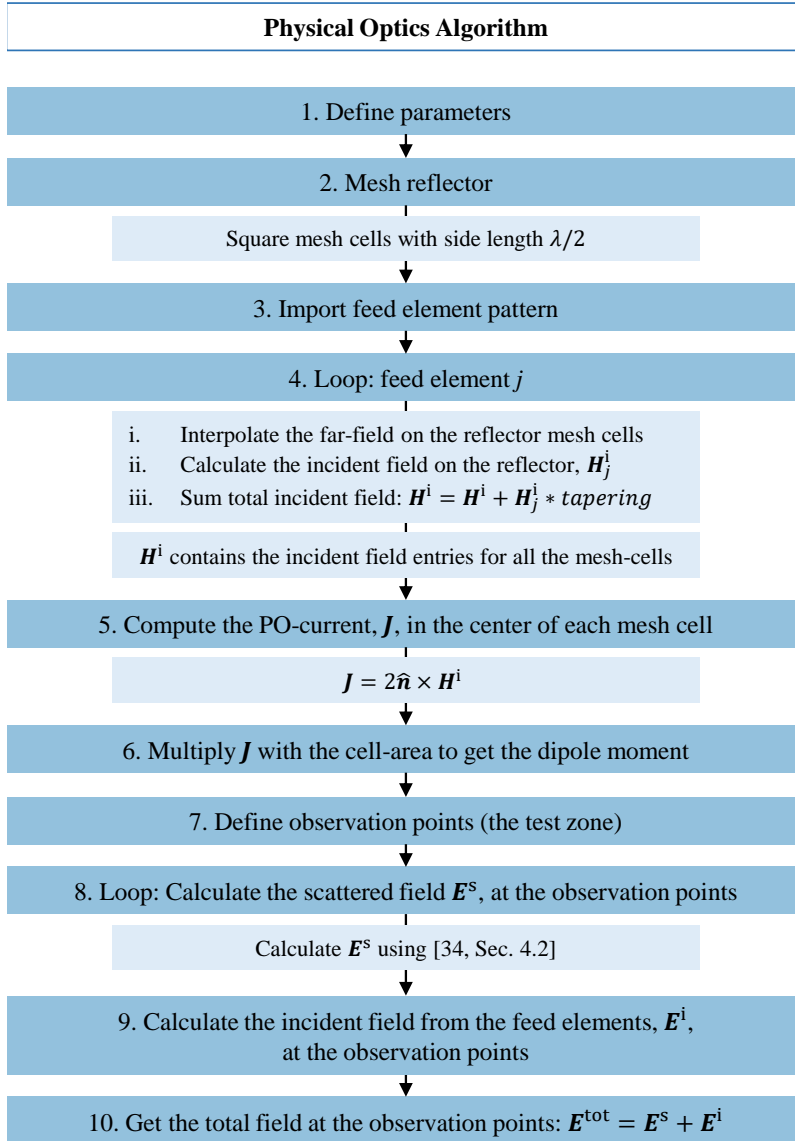
Figure 4.1: Structure of the PO algorithm used for the reflector simulations.

be seen in Fig. 3.1. The element spacing, both in vertical and horizontal direction was set to 0.11 m, which corresponds to one wavelength at 2.7 GHz. Simulations were performed both in free-space, as well as with a PEC ground plane. The ground plane was placed on the yz-plane at $x = 0$ m.

4.1.2 Physical Optics

The PO algorithm originates from the work performed in [47]. A schematic view of the algorithm is shown in Fig. 4.1. First, the parameters are defined, such as

the dimensions and the shape of the reflector, as well as the position of the antenna elements in the feed array. Second, the reflector surface is meshed, using square cells with a side length not larger than $\lambda/2$. As the third step, the embedded far-field radiation pattern of the feed array element is imported. The fourth step iterates over all elements, j, in the feed array. For every element the far-field radiation is calculated on every mesh cell of the reflector surface. On each reflector cell, the incident field, $\mathbf{H}_j^i$, from each feed element is summed together. In this step, an optional tapering can also be included. As the fifth step, the PO-current, $\mathbf{J}$, is calculated at the center of each mesh cell according to $\mathbf{J} = 2\hat{\mathbf{n}} \times \mathbf{H}^i$. In the sixth step, the PO-current is multiplied with the corresponding area to get the dipole moment for each mesh cell. The seventh step is to define the observation points, i.e., the grid points in the test zone in front of the reflector. In the eighth step, the scattered field, $\mathbf{E}^s$, from the reflector is calculated using the integral expressions in [34, Sec. 4.2]. In the ninth step, the incident field, $\mathbf{E}^i$, directly from the feed elements is calculated at the observation points. In the final step, $\mathbf{E}^i$ is added to $\mathbf{E}^s$, to obtain the total field $\mathbf{E}^{tot}$.

The observation points are located on a grid with spacing d_x, d_y and d_z, at a distance d and a height h, as shown in Fig. 3.3 and Fig. 3.4. These points represent the test zone, which can be defined as a cylindrical volume or a circular plane.

4.2 Measurements

The MoM and PO simulations were verified by measurements. For this purpose, a virtual planar array and two manufactured reflector systems were used and investigated as described in Chapter 3. The measurements were performed using a probe antenna, placed in front of the measurement system and moved along a grid, while the field was sampled. The field strength was obtained by measuring the transmission coefficient, S_{21}, between the probe antenna and the measurement system using a network analyzer. This was done for both orthogonal polarizations.

4.2.1 Virtual Planar Array

As described in Section 3.1 and in [A], the virtual UPA was synthesized by placing a vertical 8×1 ULA at different positions along a horizontal line. The spacing between the elements in the virtual ULA, both in the vertical and horizontal direction, was 0.11 m corresponding to one wavelength at 2.7 GHz. For every position, the field in front of the array was sampled by a 2.7 GHz monopole antenna mounted on a ground plane. The measurements were performed only for the vertical polarization.

The measurements were performed in an AC with the dimension 2.0 m height, 3.5 m width and 5.5 m length. The distance from the SAE/ULA/UPA to the center of the test zone was 3.7 m.

4.2.2 Sub-6 GHz Reflector

The sub-6 GHz reflector measurements in [B] were performed in a large tent at an outdoor open area test site. A 2D positioning device with step motors was used to move the probe antenna in a horizontal grid in front of the reflector system. The grid covered a circular test zone of diameter $w_t = 2.9\,\text{m}$. Additional sampling was performed for some different heights following the test verification method introduced in [E]. As probe a biconical antenna was used. Measurements were performed with the uniformly excited feed array, as well as with an amplitude tapered one; however, the latter was only measured for the vertical polarization.

The measurement results had to be post-processed to remove unwanted reflections present in the measurement setup. Behind the positioning device and in front of the reflector system, the tent fabric wall including a wooden support structure generated a reflected wave that created a ripple in the measurement results. The reflection was identified and removed from the impulse response of the measurement data, and thereafter the filtered data was transformed back to the frequency domain. Both the raw and filtered measurement data was compared to the simulated data.

4.2.3 28 GHz Reflector

The measurements for the 28 GHz system in [C], were performed in the same AC as the virtual planar array measurements. A similar positioning device was used, as for the sub-6 GHz reflector measurements, but in a smaller scale. A standard gain horn antenna was used as a probe antenna. The field was sampled within a circle in front of the reflector system, as well as additional circular cuts at different heights to generate a cylindrical volume. The total measurement volume covered a height $h_t = 0.2\,\text{m}$ and a diameter $w_t = 0.5\,\text{m}$ at a distance $d = 1.15\,\text{m}$, see Fig. 3.4.

Also for the 28 GHz system unwanted reflections were present in the measurement setup. These were identified, one as coming from a reflection from the base of the reflector and back into the feed array and a second one from the probe holder, or the probe antenna itself. The reflection at the base of the reflector and the probe holder could in practice be reduced by using RF-absorbers. However this would not solve a reflection from the probe itself. In this measurement the identified reflections were removed in the same way as for the sub-6 GHz system.

In the 28 GHz system a clear reflection was visible at the holder for the probe antenna. However, this was not the case in the sub-6 GHz measurements. A reason for this could be the size of the holder in terms of wavelengths. The holder for the 28 GHz system was $2.5\,\text{cm}$ wide, which corresponds to $2.3\,\lambda$, whereas the sub-6 GHz holder was $5\,\text{cm}$ wide, which corresponds to $0.3\,\lambda$. Another plausible explanation could be that the holder material itself is more reflective at higher frequencies. These differences would make the holder more disturbing in the 28 GHz system.

The reflection at the base of the reflector present in the 28 GHz system was not

observed in the sub-6 GHz system. It should be noted that the reflection at the base of the reflector depends on the radiation pattern of the feed array. For the 28 GHz system, the base of the reflector is more illuminated than for the sub-6 GHz system. Finally, the sub-6 GHz measurements were done outdoors, in a less controlled environment compared to an AC, which gives rise to a more noisy impulse response and makes it harder to identify different reflection contributions.

4.3 Evaluation

The simulated and measured field variations can be presented in different ways. Three representations are discussed in this section: the variations within the test zone along a parallel line (1D), in a plane (2D), and in a volume (3D). Some results, mainly from the sub-6 GHz system measurements in [B], have been selected to illustrate the evaluation. Additional and more complete results can be found for the virtual planar array and 28 GHz system in [A] and [C], respectively.

4.3.1 1D Variation

In Fig. 4.2, the simulated and measured normalized power for the sub-6 GHz system are plotted along a line in y-direction. This was done for easier comparison and a better understanding of the peak-to-peak variation of the field. The corresponding phase variation is shown in Fig. 4.3. The simulated and measured curves have the same behavior, but the latter shows larger variations. It should be noted that an ideal plane wave, would have no variations in amplitude and phase along this line.

The peak-to-peak variation of the power is around 3 dB for both the tapered and non-tapered feed array when $y \in [-1\,\mathrm{m}, 1\,\mathrm{m}]$. In the same interval, the phase has a peak-to-peak variation of 30° for the non-tapered feed array and 15° for the tapered feed array. However, when reducing the interval to $y \in [-0.75\,\mathrm{m}, 0.75\,\mathrm{m}]$, the non-tapered feed array system has still a peak-to-peak variation for the power of 3 dB, whereas the system with the tapered feed array improves and varies less than 1.3 dB.

For the 28 GHz system a very similar peak-to-peak performance as the sub-6 GHz system is achieved. Only a non-tapered feed array was evaluated in this case, and similar peak-to-peak variation is achieved as for the non-tapered feed array in the sub-6 GHz system, but for a smaller width. The same performance was achieved for $y \in [-0.15\,\mathrm{m}, 0.15\,\mathrm{m}]$ in the 28 GHz system, as for $y \in [-1\,\mathrm{m}, 1\,\mathrm{m}]$ in the sub-6 GHz system.

4.3.2 2D Variation

The simulated and measured field variations in terms of normalized power P over a yz-plane in front of the sub-6 GHz are shown in Fig. 4.4. The figures have been nor-
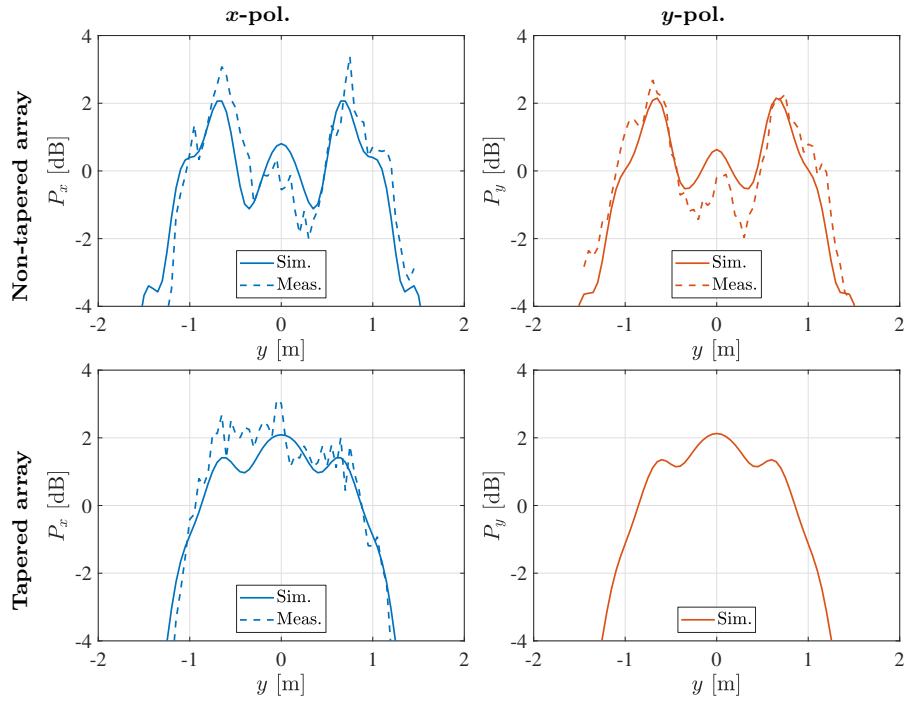
Figure 4.2: Sub-6 GHz system, simulated and measured normalized power P along the line y, at $h = 1.4\,\mathrm{m}, d = 4\,\mathrm{m}$, for the vertical (x) and horizontal (y) polarization at $2\,\mathrm{GHz}$ [B].
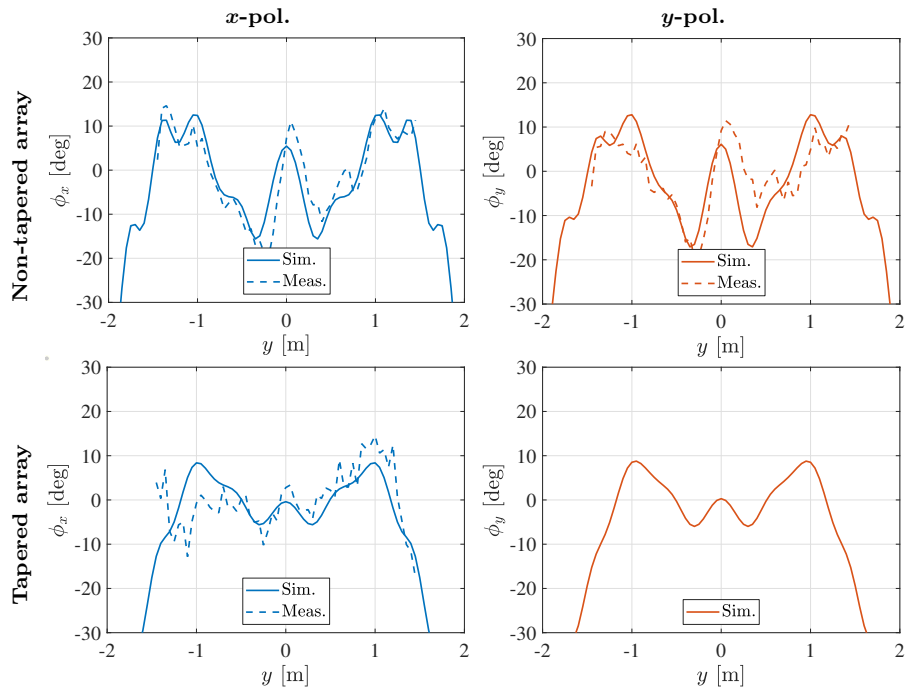
Figure 4.3: Sub-6 GHz system, simulated and measured normalized phase ϕ along the line y, at $h = 1.4\,\mathrm{m}, d = 4\,\mathrm{m}$, for the vertical (x) and horizontal (y) polarization at $2\,\mathrm{GHz}$ [B].
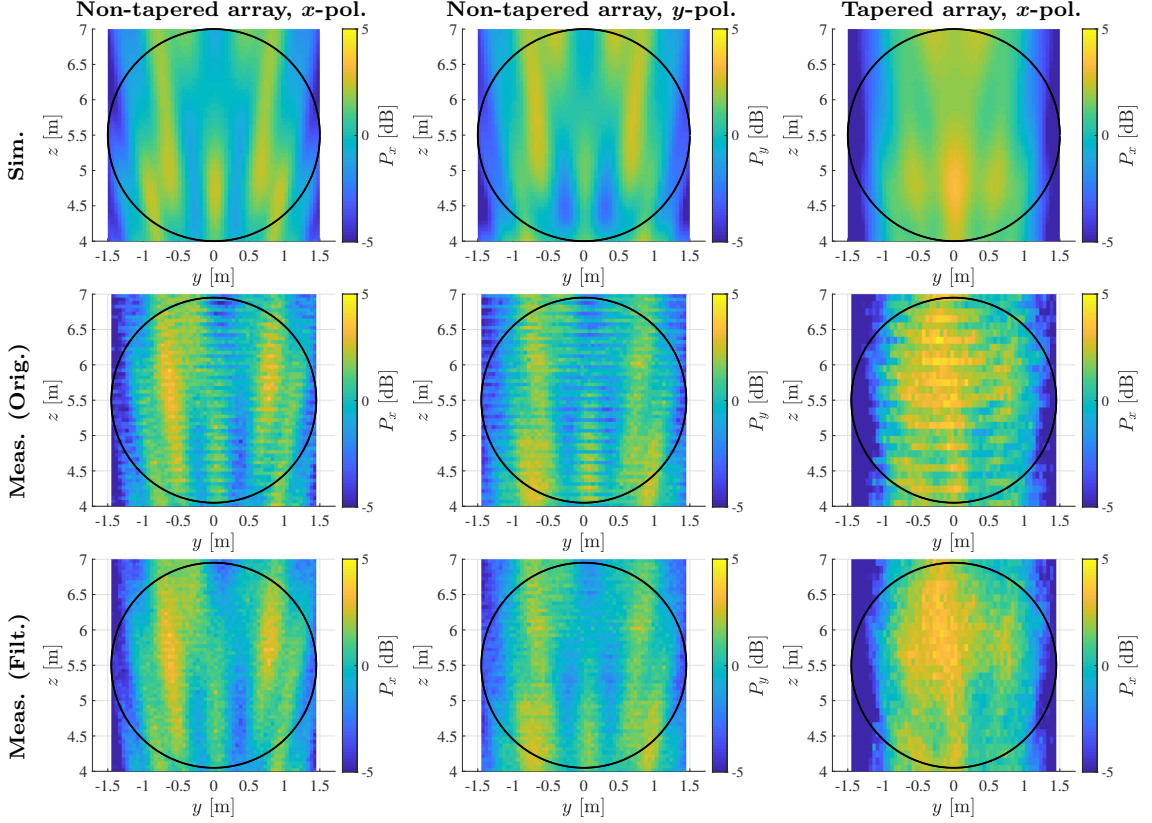
Figure 4.4: Sub-6 GHz system, simulated and measured (both original non-filtered and filtered) normalized power P for the vertical (x) and the horizontal (y) polarizations, in the yz-plane at height $h = 1.4$ m and $f = 2$ GHz [B].

malized to their mean value, for easier comparison. The measured data is shown both for the original as well as the filtered measured data, where the identified reflections have been removed. The good agreement between simulated and measured filtered data should be noted. Moreover, a smoother and lower field variation is achieved for the tapered feed array measurements.

The field variations within the test zone can be summarized in terms of standard deviation (STD). The STD, σ_{dB}, of the normalized power P, can be expressed as follows [54]

$$\sigma_{\mathrm{dB}}(P) = 5 \log\left(\frac{1 + \sigma(P)}{1 - \sigma(P)}\right) , \tag{4.1}$$

where σ is the STD of the normalized power in linear units, i.e.,

$$\sigma(P) = \sqrt{\mathrm{VAR}\left\{\frac{P}{\mathrm{MEAN}\{P\}}\right\}} , \tag{4.2}$$

where $\mathrm{VAR}\{\cdot\}$ and $\mathrm{MEAN}\{\cdot\}$ are the sample variance and mean operations, respectively.
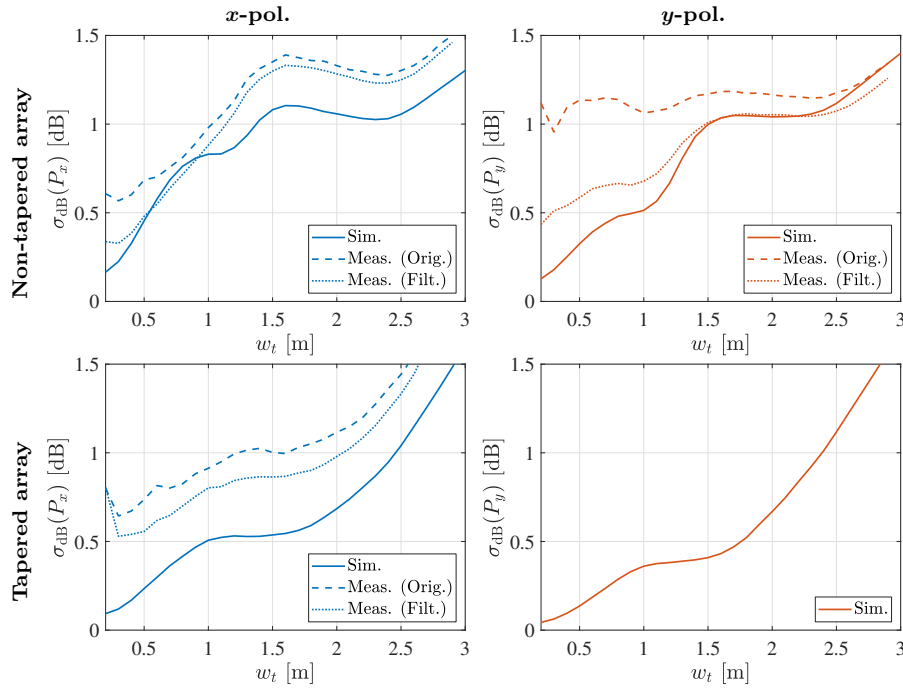
31

Figure 4.5: Sub-6 GHz system, simulated and measured STD, $\sigma_{\mathrm{dB}}(P)$, of the normalized power P as a function of the circular test zone diameter w_t, at $h = 1.4\,\mathrm{m}$, $d = 4\,\mathrm{m}$ at $2\,\mathrm{GHz}$ [B].

A plane wave propagates with a phase factor, e^{-jkz}, where $k = 2\pi/\lambda$ is the wavenumber. Therefore, to better show how the phase varies compared to the plane wave, the theoretical variation of the phase in the propagation direction was removed. This was done for both the simulated and measured data. Thereafter, the STD of the phase, $\sigma(\phi)$, was calculated using Eq. (4.2), where P has been exchanged for the phase ϕ.

The $\sigma_{\mathrm{dB}}(P)$ for the sub-6 GHz system is shown in Fig. 4.5, for a circular test zone, including results for both polarizations as well as a tapered feed array. A simulated STD of around 1 dB can be achieved for a test zone diameter of up to 2.5 m, a similar performance is achieved for the measured data for the horizontal polarization. However, a slightly larger variation, around 0.3 dB, for the measurement results for the vertical polarization is obtained. An improvement is given using the tapered feed array for diameters smaller than 2.5 m. At the diameter 1.5 m, an STD of 0.5 dB for the tapered feed array is achieved, whereas the corresponding value for the non-tapered feed array is 1 dB.

The STD of the power for the SAE, horizontal ULA and the UPA are shown in Fig. 4.6 as a function of the circular test zone diameter. The measured data is compared to simulated data, performed both in free-space, but also including a PEC as ground plane. The PEC ground plane is located in the yz-plane at $x = 0\,\mathrm{m}$. It
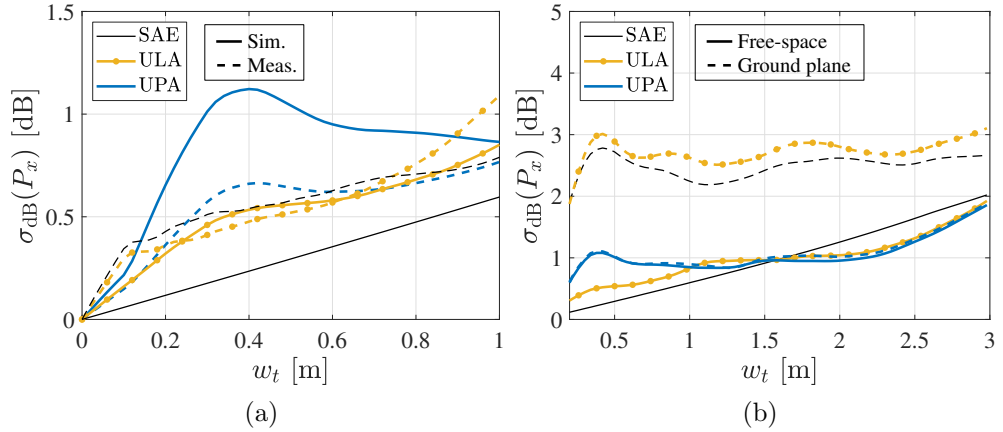
Figure 4.6: Virtual planar array, STD within the circular test zone as a function of the diameter. Results are shown for the SAE, horizontal ULA and UPA antenna, as shown in Fig. 3.1. (a) The STD for the simulated and corresponding measured data. (b) STD for the simulated free-space and PEC ground plane case.

can be clearly seen that with the presence of a ground plane, there is a considerable increase in the STD for the ULA and the SAE, but not for the UPA. As expected, the ground reflection gives rise to constructive and destructive interference in different locations of the test zone. With the planar array, there is less radiation towards the ground and therefore less reflection and a better performance can be achieved.

4.3.3 3D Variation

In Fig. 4.7, $\sigma_{\mathrm{dB}}(P)$ is shown for the 28 GHz system, including the STD for a cylindrical test volume and not just a circular plane. Here it can be seen that the variations increase slightly in a test volume, compared to a plane, but are still below an STD of 1.5 dB for a cylinder with diameter 0.3 m and height 0.2 m.

From the STD results in Fig. 4.5, Fig. 4.6 and Fig. 4.7 we can conclude at which test zone diameter the variations start to drastically increase. For the two reflector systems this occurs when the test zone diameter reaches around 75 % of the feed array width, L_f, see Fig. 3.3 and Fig. 3.4. However, for the UPA, we get the increase around 85 % of the planar array width, L_h.

A difference in the comparison between the measurement and simulation data for the two reflector systems can be observed. The measurement data for the sub-6 GHz system is consistently above the simulated STD curve, whereas the opposite is true for the 28 GHz system. First, it must be noted that the measurements for the sub-6 GHz system were performed in an outdoor open area test site, whereas the 28 GHz measurements were performed inside an AC. The AC is a more controlled environment compared to the outdoor test site, and thus more accurate data is expected. However, in the 28 GHz measurements, a large probe antenna in terms of
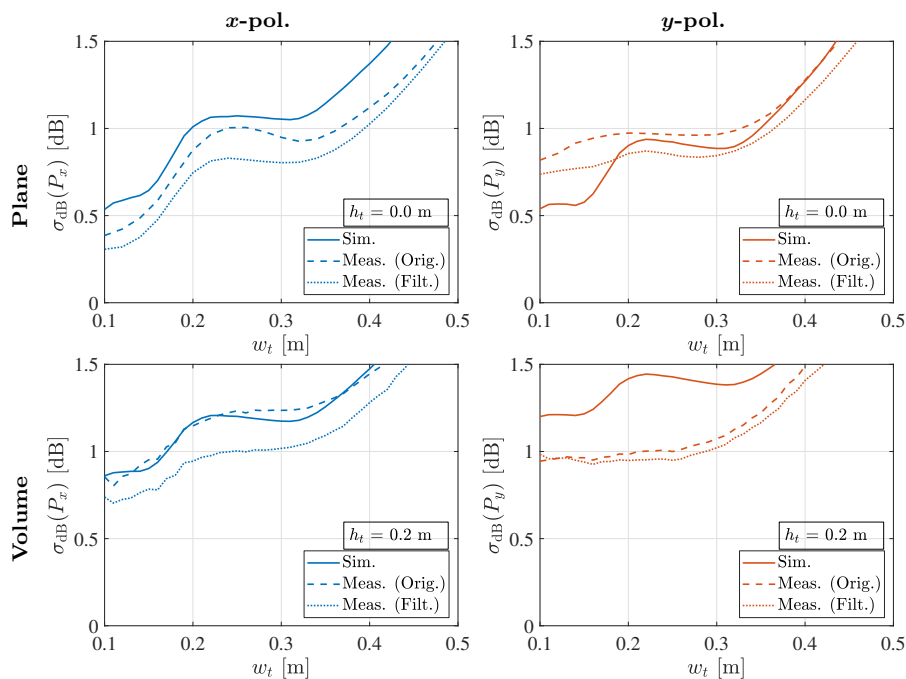
Figure 4.7: 28 GHz system, simulated and measured STD of the normalized power P as a function of the test zone diameter, w_t, at 28 GHz [C]. The test zone is located at $h = 0.3$ m and $d = 1.15$ m, for both the plane and the volume.

wavelengths was used. The aperture size of the standard gain horn antenna for the 28 GHz measurements was 53.7 mm × 73.1 mm, whereas the biconical antenna used for the sub-6 GHz measurements had the dimensions 49 mm × 140 mm. These corresponds to $5\lambda \times 7\lambda$ and $0.3\lambda \times 0.9\lambda$, respectively. Ideally, a probe antenna would be a point; however, this is not possible and it will have a physical dimension. The dimension for the standard gain horn antenna is larger in terms of wavelengths, which results in an averaging of the field over a much larger area in terms of wavelengths than for the other probe antenna. This can cause lower measured variation than what actually is the case.

4.4 Test Zone Verification Procedure

The measurements presented were very time-consuming to perform. Therefore, a simple way to verify that the system is working as intended is needed. For this purpose, a test zone verification procedure was presented in [E]. The paper is based on simulations of the sub-6 GHz reflector system and compares three different procedures for sampling the field within a circular test zone, see Fig. 4.8.

As a reference, a dense uniform grid comparable to the results discussed in Section 4.3.2 was used. This reference grid was compared to data points sampled along
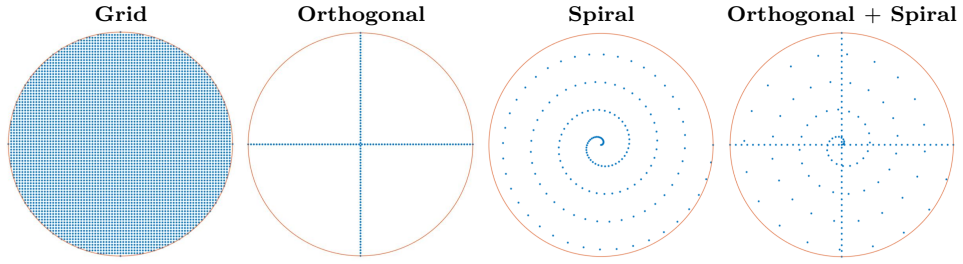
Figure 4.8: Four different ways of sampling the data points within the test zone [E]. The four methods are the grid, the two orthogonal lines, the spiral and a combination of the two orthogonal lines and the spiral.
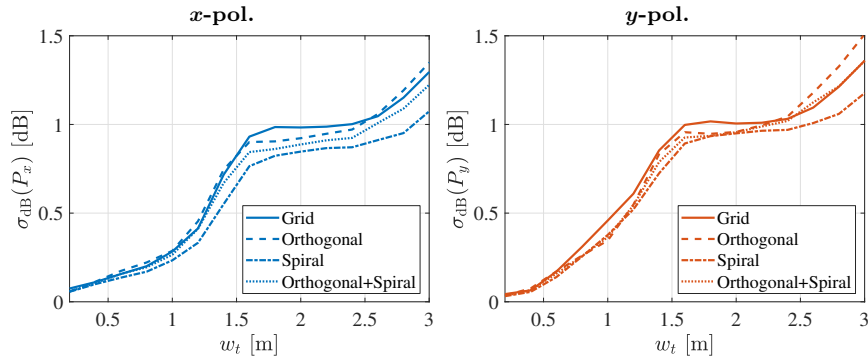

Figure 4.9: Sub-6 GHz system, STD as a function of circular test zone diameter for the different sample methods presented in Fig. 4.8. The comparison is presented for $d = 4.5$ m and $f = 2.1$ GHz.

two orthogonal lines, along a spiral-shape as well as a combination of the two lines and the spiral. A comparison in terms of STD is shown in Fig. 4.9. From these results it can be seen that all three methods perform well, i.e., they give approximately the same STD. Therefore it is possible to choose the verification method based on which is the most convenient and time-efficient.

Parts of the measurements in [B] were sampled by using the two orthogonal line procedure. This was done to reduce the measurement time for validating the variations in the test zone volume of the system.

Chapter 5

Measurements in the Random-LOS Environment

The random-LOS measurement systems have now been described in detail in the previous chapters. The main application of the systems is to perform passive and active measurements of antennas and wireless devices. This chapter describes how these measurements can be performed in practice. The two reflector systems are considered, since the planar array was not physically realized other than as a virtual planar array.

The random-LOS measurement setup consists of the reflector and feed system, turntable/positioner, AUT or DUT, instrument, and control computer. The turntable or positioner will rotate the AUT or DUT in front of the reflector system during the measurements. The measurements presented in this chapter are all performed in a 2D plane. However, also 3D performance can be measured, either by using a 3D positioner for smaller devices or tilting the reflector system. Tilting the reflector system can work for some slight elevation angles in cases where the DUT, e.g., a vehicle, cannot be rotated in 3D. Such measurements would result in a partial 3D measurement. The type of instrument used depends on the measurements. For passive measurements typically a network analyzer is employed, whereas active measurements use a communication tester. The turntable/positioner and instrument is controlled by a computer, which also collected the measurement data from the instrument. For some of the measurements, some additional parts are included in the setup.

5.1 Passive Measurements

Passive measurements typically consider radiation pattern and gain of the AUT. However, calibrating the system for active measurements, to extract absolute gain and correct power levels fall also into this category. Moreover so are the measurements to verify the field variations in front of the reflector systems as described in Section 4.2.
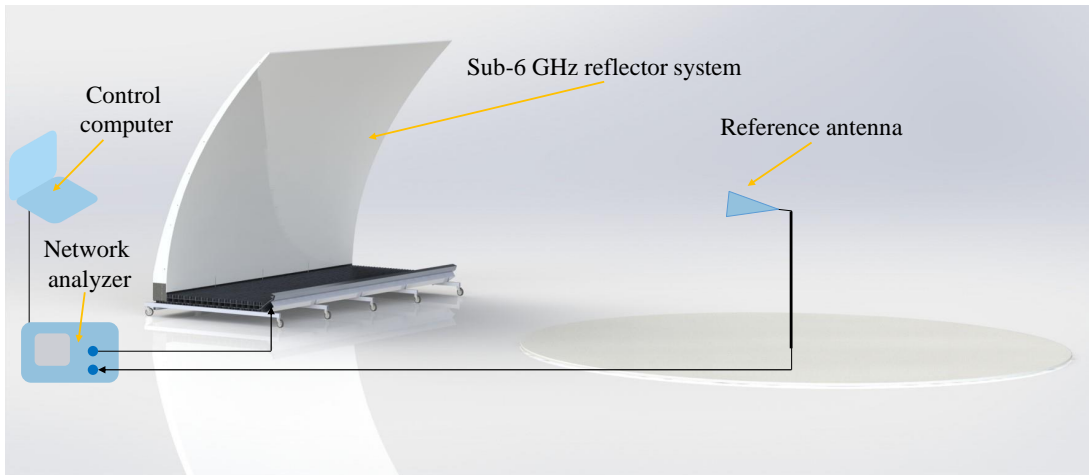
Figure 5.1: Schematic view of the reference measurement setup for the sub-6 GHz system.

Those measurements are in passive mode, and are performed to calibrate and to check that the system works as intended. A faster, but slightly less accurate, way to verify the system is to use the test zone verification procedure described in Section 4.4. Both methods verify the field variations by moving a probe antenna in a grid pattern in front of the reflector system, while the transmission coefficient, S_{21}, is measured.

5.1.1 Reference Measurements

The reference measurements are performed using an antenna designed for the applicable frequency band and with known gain. The reference antenna is placed in the center of the turntable, or is mounted on the positioner, at the same location as the DUT will be placed. The reference antenna should point directly to the center of the reflector and the transmission coefficient should be measured using a network analyzer. A schematic view of the reference setup for the sub-6 GHz system is shown in Fig. 5.1. The setup is very similar for the 28 GHz system; however, in this case a 3D positioner can be used for holding the smaller DUT.

A reference signal power level is measured for each polarization. The reference measurements give the losses in the system, so as to calibrate them away for the actual measurements. The reference measurement will contain the losses from the reflector system, the free-space losses between the reflector system and the reference antenna, and the reference antenna itself. The known gain for the reference antenna is then removed from the reference measurement data. Additional cables that are later used in the actual measurements should be accounted for to get the proper gain values. In the case of using long cables, additional power amplification might be needed. During the reference measurement, additional care should be taken such that no unwanted reflections are present in the measurement setup, e.g., reflections
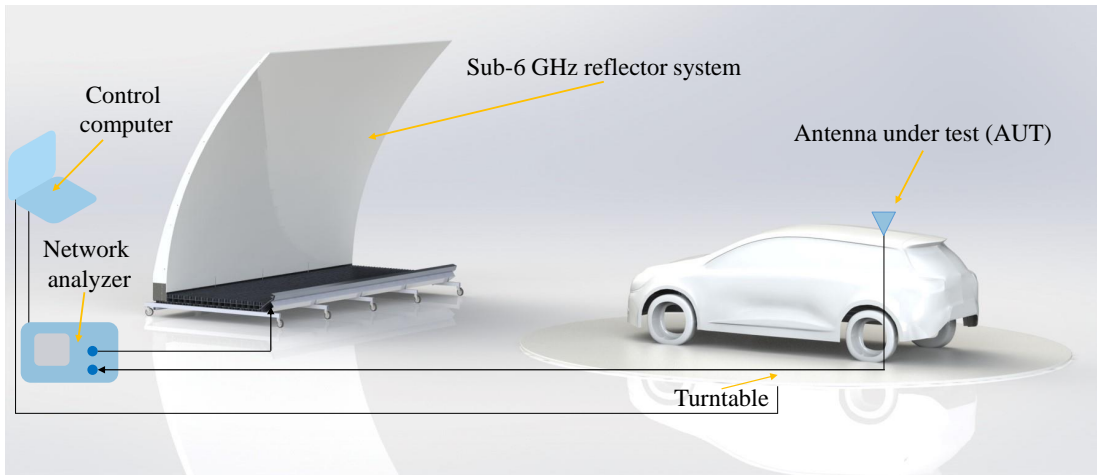
Figure 5.2: Schematic view of the passive measurement setup for vehicles, using the sub-6 GHz system.

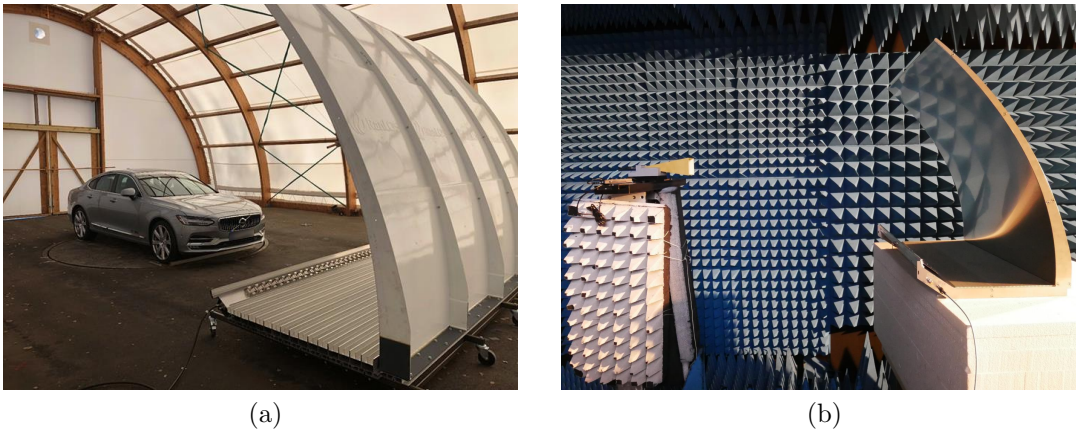|	
(a)	(b)

Figure 5.3: Pictures of passive measurement setups. (a) Setup for vehicles, using the sub-6 GHz system. (b) Setup for smaller devices, using the 28 GHz system.

from the positioning device, surrounding objects, or unstable cables.

5.1.2   Setup for Passive Measurements

To measure the radiation pattern of an AUT, a very similar setup to the one described in Section 5.1.1 is used. The AUT is placed in the center of the turntable or mounted on the positioner. For a schematic view of a passive measurement setup, using the sub-6 GHz system, see Fig. 5.2. Pictures of the passive measurement setup using the sub-6 GHz and 28 GHz systems are shown in Fig. 5.3. The setup for the sub-6 GHz system is shown inside a large tent at an outdoor open area test site, measuring a vehicle. The setup for the 28 GHz system is shown for measuring a standard gain
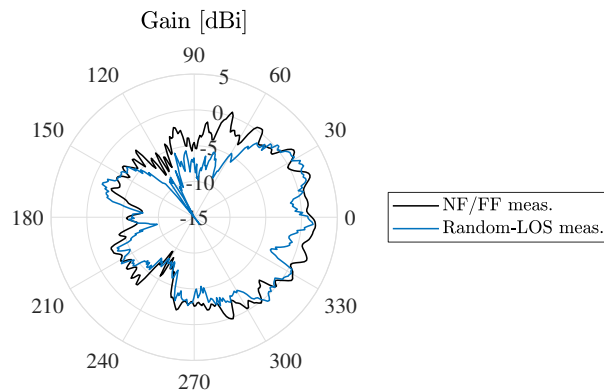
Figure 5.4: Radiation pattern measurement results in terms of gain as a function of the azimuth angle for a roof-mounted prototype shark-fin antenna on a vehicle at $2\,\mathrm{GHz}$ using the sub-6 GHz system [B]. Comparison data is shown using an NF/FF method.

horn in an AC.

In a radiation pattern measurement, S_{21} is measured for every desired angle using a network analyzer. If speed is important, the measurements can be performed while continuously rotating the turntable. However, the angular velocity is limited by the sweep time of the network analyzer. The measurement can be performed for the desired polarization, using one of the two polarizations of the random-LOS system. The AUT should be placed within the test zone of the system, in order to obtain accurate measurement results.

5.1.3   Passive Measurement Results

Radiation pattern measurement results for a roof-mounted prototype shark-fin antenna on a vehicle using the sub-6 GHz system are shown in Fig. 5.4. The radiation pattern for the antenna is shown in terms of absolute gain, where a reference measurement has been performed, as described in Section 5.1.1, using a biconical antenna. The position when the vehicle is facing the reflector, as in Fig. 5.3(a), corresponds to the azimuth angle 180° in Fig. 5.4. The comparison in Fig. 5.4 is done against the same DUT measured in an NF/FF setup. The NF/FF measurements were performed one year earlier than the random-LOS measurements and limited information on the setup and procedure are available.

The radiation gain pattern obtained with the random-LOS setup has a similar shape to the pattern obtained by an NF/FF range, see Fig. 5.4. However the absolute gain values agree better for angles around 0° and 180°, which corresponds to the vehicle facing the reflector from the back and the front, respectively. The main reason is that the AUT was not centered on the turntable, due to the small size of the turntable (4 m diameter) relative to the size of the vehicle. This causes a rotation of the AUT on a circle with a radius of 1.5 m. Additionally, the reflector was a little
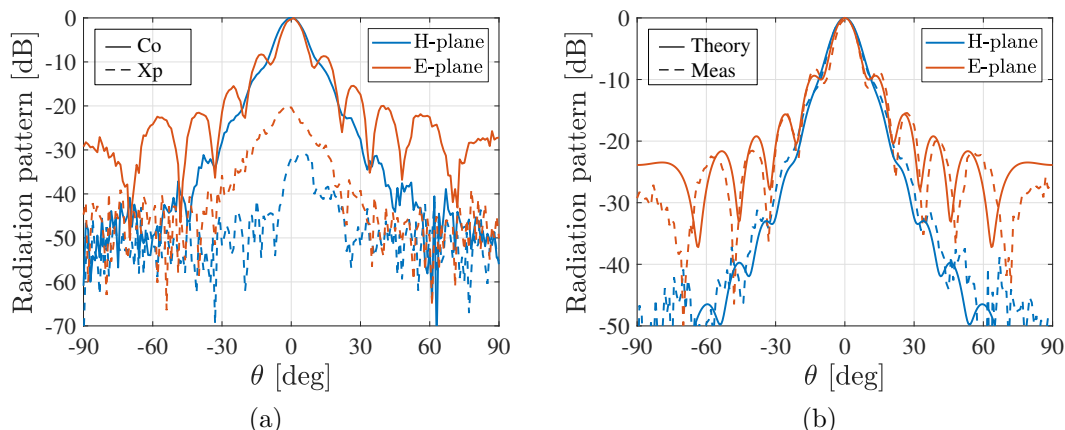
Figure 5.5: Radiation pattern measurement results at 28 GHz for a standard gain horn using the 28 GHz random-LOS measurement setup [C]. (a) Co- and cross-polar measurement results. (b) Measured and theoretical E- and H-plane results.

off-centered relative the center of the turntable. As a result, as the AUT was rotated to angles close to 90°, it was moved out of the test zone.

To evaluate the difference between the two measured radiation patterns, the mean squared error (MSE) between the NF/FF and random-LOS measurement was calculated according to

$$\text{MSE} = \frac{1}{n} \sum_{i=1}^{n} (X_i - Y_i)^2 \ , \tag{5.1}$$

where X_i and Y_i are the NF/FF and random-LOS absolute linear values of the radiation pattern, respectively. The number of angles included in the sum is denoted by n. Including all the measured angles, 0°–360°, the MSE becomes 3.7%. An improved MSE of 1.7% could be achieved, when excluding the angles in the interval 45° to 135°.

Radiation pattern results for a standard gain horn antenna using the 28 GHz system are shown in Fig. 5.5. The standard gain horn measurements shown in Fig. 5.5 are normalized to the maximum, and not shown in absolute gain. The comparison is done to the theoretical standard gain horn pattern. The MSE was calculated using Eq. (5.1), with X_i as the theoretical and Y_i as the random-LOS measured radiation pattern. The MSE is 0.12% for the E-plane and 0.02% for the H-plane, in the angle interval ±90°. If reducing the angle interval to ±45°, the MSE values become 0.08% for the E-plane and MSE = 0.02% for the H-plane. From the results in Fig. 5.5, it can be seen that the cross polarization level of the 28 GHz system is 20 dB below and that the measured results follow the theoretical results well.
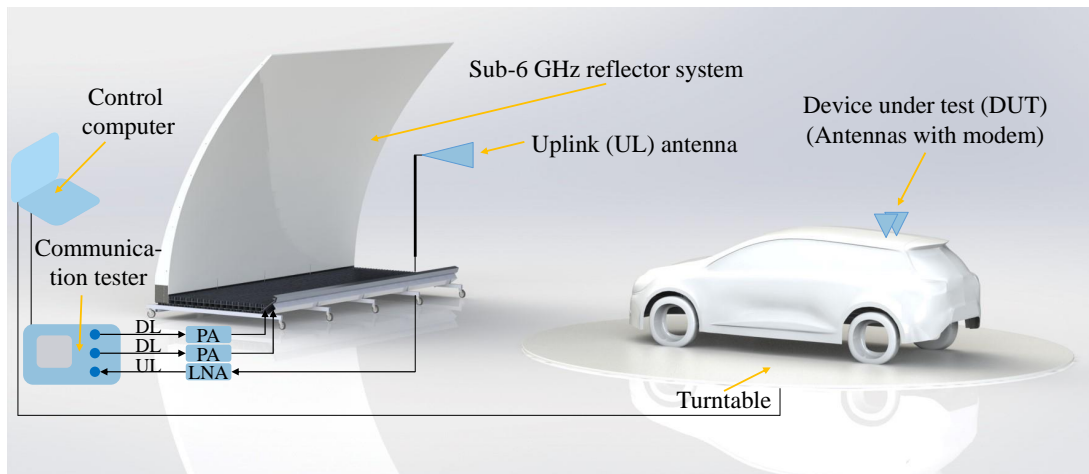
Figure 5.6: Schematic view of the active measurement setup for vehicles, using the sub-6 GHz system.

5.2   Active Measurements

In active measurements the modem, the antennas and the whole device are included in the DUT. Typically, a communication tester is used to simulate the behavior of a base station that connects to the modem in the device. A common type of active measurements is downlink TPUT measurements, where the transmission data rate is measured as a function of the received power. Active measurements are demonstrated here for long term evolution (LTE), using the sub-6 GHz setup.

For one random-LOS system, up to two transmit streams can be used, i.e., $\max(M_t) = 2$. This means that the system can support up to 2×2 polarization MIMO, where the two streams are based on one stream for each polarization [10].

5.2.1   Setup for Active Measurements

A schematic view of an active measurement setup using the sub-6 GHz system is shown in Fig. 5.6, with the corresponding picture of the setup shown in Fig. 5.7. The figure shows a 2×2 MIMO setup of a two port roof-mounted antenna on a vehicle. For a SISO measurement setup, only one of two ports on the reflector system and only one antenna port on the DUT would be used. For a SIMO measurement still only one port on the reflector system would be used, but several antennas on the DUT would be enabled. For a MISO measurement, both ports on the reflector system would be used, but only one antenna port would be enabled on the DUT.

Depending on the measurement settings, i.e., the measurement type and the modulation used, power amplifiers (PAs) might be needed in the downlink. The PAs are needed to get high enough power levels at the receiver. A separate uplink (UL) antenna is also needed to keep the connection to the modem. In Fig. 5.6 and Fig. 5.7

Figure 5.7: Picture of the active measurement setup for vehicles, using the sub-6 GHz system [B].

the UL antenna is placed on the side of the reflector system to avoid blockage of the measurement. Other positions of the UL antenna are possible, as long as it does not interfere with the radiated field from the reflector. The signal in the UL is amplified using a low noise amplifier (LNA). The need of an LNA in the uplink depends on the receive sensitivity of the communication tester.

Reference measurements are needed to get the correct power levels for the active part. The reference measurements are performed, without the vehicle, as described in Section 5.1.1. The cables and PAs used during the active measurements, but not included in the reference measurement, need to be accounted for. The external attenuation, the attenuation between the communication tester and the DUT that is calculated from the reference measurement including the potential extra cables and PAs, is then loaded into the communication tester. Note, when using both ports on the reflector system, a different attenuation value will be needed for each port. This requires that a reference measurement is performed for each polarization, i.e., each port on the reflector system.

Before a measurement can be started, the communication tester needs to have a connection with the DUT. To achieve this connection, it can be easier to start with a low modulation and then change it to the one needed for the measurements.

A downlink TPUT measurement is performed by sweeping the power level from high to low, while measuring the TPUT received at the DUT. Such a sweep is performed for every rotation angle on the turntable. The number of rotation angles depends on the wanted angular resolution. The TPUT results presented in Section 5.2.2 are calculated from power sweeps performed for every 5° on the turntable. It is also possible to rotate the turntable and DUT continuously, while measuring
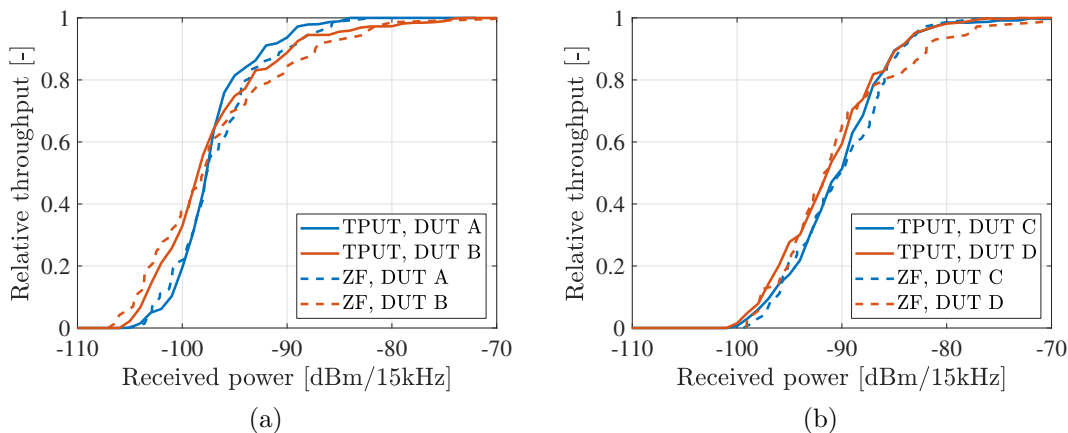
Figure 5.8: TPUT measurement results for 2×2 MIMO on full vehicle using the sub-6 GHz system [B]. (a) TPUT for LTE band 3. (b) TPUT for LTE band 7.

the TPUT for one power level per whole 360° turn. However, this depends on the limitations of the turntable and has to be investigated further.

For every rotation angle on the turntable a TPUT threshold will be achieved according to Fig. 2.2. The steep threshold is explained by the static environment. During the measurements, it is essential to keep the connection between the communication tester and DUT. To achieve this, the power sweep is stopped when the zero TPUT level is reached at every angle. The steep throughput curves for every measured angle are combined by calculating the average TPUT for every power level.

5.2.2   Active Measurement Results

TPUT measurement results for roof-mounted antennas using 2×2 MIMO, LTE transmission mode 3, are shown in Fig. 5.8. The measurements are performed for two different LTE bands, band 3 and 7, with two different antennas for each band. The active measurement results are compared to those obtained from post-processing the 2×2 passive radiation pattern for the same vehicle-antenna setup. Although the spatial multiplexing scheme of the receiver modem is unknown, we have compared the measured TPUT to a ZF receiver to get an idea of how they match up. This is done by creating the **H**-matrix from the radiation pattern measurements and use Eq. (2.4) to create the ZF data. Since the 2×2 MIMO performance was wanted, the worst of the two diagonal entries in Eq. (2.4) was set as corresponding to the ZF performance. The ZF curves have been normalized, where a more detailed description is given in [B]. Similarities in the TPUT and ZF curves can be seen in Fig. 5.8.

It should be noted that the antennas mounted on the roof of the vehicle were all vertically polarized antennas. The random-LOS environment employs polarization MIMO, with two orthogonally polarized streams [10]. In this case, one of the streams

will be related to the cross-polarization level of the measured antenna.

Chapter 6

Contributions and Future Work

The continuous evolution of communication systems, with the increase in type and number of wireless devices and a shift towards higher frequencies, requires also advances in device testing. How the testing should be performed depends on the specific application, e.g., the user environment and the device size. However, it is not only those areas that determine which is the *best* option of testing for a certain scenario. Other factors such as relevance, measurement time, implementation feasibility, reliability, and cost-efficiency are also of fundamental importance. This thesis covers the random-LOS measurement system and how it could be one of the options for current and future testing of wireless devices. This chapter summarizes the thesis and provides the contributions and some suggested future work directions.

6.1 Contributions

The contributions of the thesis are related to the development of the new random-LOS measurement concept. The main contributions cover different aspects of the random-LOS environment and systems and are described in the following list:

- **Random-LOS measurement system using a virtual planar array**
  The concept of a random-LOS system employing a UPA with 8×23 elements was evaluated. Simulations were compared with measurements using a virtual planar array. The analysis shows that a plane wave can be generated with good accuracy, e.g., an STD of the power of $0.8\,\text{dB}$ within a circular test zone with a diameter of $1\,\text{m}$. The performance analysis in a simulated environment with a PEC ground plane was evaluated for the SAE, horizontal ULA, and UPA, where the UPA showed considerably better performance than the other two.

- **Random-LOS measurement system for sub-6 GHz**
  A novel random-LOS reflector system for the 1.5–$3\,\text{GHz}$ system has been designed and measured. The system has been developed to characterize devices

mounted on vehicles, or in general devices of larger form factors. A power STD of 1 dB was achieved for a circular test zone with a diameter of 2.5 m. It was shown that a considerable improvement of the test zone could be achieved by employing a tapered feed array, where an STD of 0.5 dB was achieved for a test zone diameter of 1.5 m.

- **Random-LOS measurement system for 28 GHz**
  A compact random-LOS reflector system operating at the 28 GHz band was designed, manufactured and measured. The simulations and measurements were shown to be in good agreement. For this system, an STD of less than 1.5 dB was achieved for a cylindrical test zone of diameter 0.3 m and height 0.2 m. 5G antenna systems and devices, operating at the 28 GHz band, can be measured in this type of setup.

- **Active vehicular measurements with the random-LOS system**
  The first active device measurements have been performed using the sub-6 GHz system. The roof-mounted antennas on a vehicle were tested with respect to the LTE transmission mode 3, evaluating the 2×2 MIMO system performance. Good agreement was obtained between the measured TPUT data and the theoretical model based on the radiation pattern of the antennas with a ZF receiver.

- **Test verification procedure**
  A procedure for decreasing the needed number of samples within the test zone in order to estimate the STD has been proposed. Three different methods for sampling the field in the test zone are introduced: along a cross, a spiral, and a combination of these two ways. This procedure can reduce the measurement time for estimating the STD within the test zone for a random-LOS system, while still keeping the accuracy.

As seen in the list above, the research work has contributed to the development of the random-LOS measurement technique. All the contributions are important and valuable steps forward in the continuous development towards a cost-effective, easy to use and reliable test method.

6.2   Future Work

The random-LOS measurement system is in its early development phase and there are many different areas that can be considered for future work. In the following section some of the possible paths will be mentioned. The suggestions are mainly focused on the reflector systems, since those have been physically realized and have shown to be more cost effective to manufacture and more flexible than the planar array system.

An improvement of the system in terms of reduced field variation within the test zone should be considered. This is important for the overall accuracy of the system, both for passive and active measurements. For the 28 GHz system, amplitude tapering of the elements in the feed array could be used. The possibility of performing some edge treatment of the reflector, in order to reduce the diffraction from the edges, could be evaluated. To improve the accuracy of the system the illumination of the bottom of the reflector, which creates a reflection back in to the feed array, should be removed. The problem of illuminating the base of the reflector was visible for the 28 GHz system, and could be removed by redesigning the feed array to reduce the illumination of the reflector base. Other ways to solve this issue could be to mount absorbers on the bottom of the reflector.

The trend of moving towards higher frequencies with the introduction of 5G means that there are many new frequency bands that will be introduced in the close future. This makes it important to look into extending the 28 GHz random-LOS measurement systems to other bands. The main work would be to design new feed arrays or redesign the current one, to cover other or more frequencies. An investigation regarding the reflector performance at higher frequencies should also be considered.

Testing of additional frequency bands is of interest for the sub-6 GHz system. The current system has a working frequency of 1.5–3 GHz, but other frequency bands are possible by exchanging the feed array. With two scaled versions of the current 1.5–3 GHz feed array, the frequency range of 0.75–6 GHz can be covered. However, the system is not limited to this frequency band, and other frequencies are also of interest.

The testing of the sub-6 GHz system has been performed in an outdoor open area test site, which has a less controlled environment than a semi-AC. Additional measurements of the repeatability and reproducibility of the system are important, and preferably these would be performed in a semi-AC. Evaluating measurements for other 2D cuts, for example by tilting the system or tilting the DUT, is also interesting.

The active measurement performance using the sub-6 GHz systems should be tested further, and a full accuracy budget should be made and compared to other measurement methods. This also includes tests where the antennas are placed in different locations on the DUT. The active measurements presented in this thesis have been performed with a stepped turntable movement. Using a continuous movement for speeding up the measurements should be investigated. All these aspects are important to reach a better understanding of the strengths and the limitations of the system. Active measurements should also be performed for smaller 28 GHz units, using the 28 GHz setup.

The real-life hypothesis still remains to be proven. A future possibility would be to investigate the validity of the hypothesis, by means of comparing measurements and simulations in RIMP, random-LOS, and different real-life scenarios.

As can be seen, several challenges and research opportunities still lie ahead in the pursuit of affordable and practical device measurements for future wireless applica-

tions.

References

[1] 3GPP, "Verification of radiated multi-antenna reception performance of user equipment (UE)," 3rd Generation Partnership Project, Technical Report 37.977 V15.0.0, Sep. 2018.

[2] P.-S. Kildal and J. Carlsson, "New approach to OTA testing: RIMP and pure-LOS reference environments and a hypothesis," in *2013 7th European Conference on Antennas and Propagation (EuCAP)*, Apr. 2013, pp. 315–318.

[3] J. Carlsson, "WSAP - wire structure analysis program, a method of moments wire structure analysis program," available: jan.carlsson@provinn.se.

[4] S. M. Moghaddam, A. A. Glazunov, and J. Yang, "Wideband dual-polarized linear array antenna for random-LOS OTA measurement," *IEEE Transactions on Antennas and Propagation*, vol. 66, no. 5, pp. 2365–2373, May 2018.

[5] A. Paulraj, R. Nabar, and D. Gore, *Introduction to Space-Time Wireless Communications*. Cambridge University Press, May 2003.

[6] H. T. Friis, "A note on a simple transmission formula," *Proceedings of the IEEE*, May 1946, publisher: Institute of Electrical and Electronics Engineers (IEEE).

[7] C. A. Balanis, *Antenna Theory: Analysis and Design*. Hoboken, USA: John Wiley & Sons, Incorporated, 2016.

[8] A. Goldsmith, *Wireless Communications*. Cambridge University Press, Aug. 2005.

[9] E. Telatar, "Capacity of multi-antenna Gaussian channels," *European Transactions on Telecommunications*, vol. 10, no. 6, pp. 585–595, 1999.

[10] A. Razavi, A. A. Glazunov, P.-S. Kildal, and J. Yang, "Characterizing polarization-MIMO antennas in random-LOS propagation channels," *IEEE Access*, vol. 4, pp. 10 067–10 075, 2016.

References

[11] P.-S. Kildal, A. Hussain, X. Chen, C. Orlenius, A. Skårbratt, J. Åsberg, T. Svensson, and T. Eriksson, "Threshold receiver model for throughput of wireless devices with MIMO and frequency diversity measured in reverberation chamber," *IEEE Antennas and Wireless Propagation Letters*, vol. 10, pp. 1201–1204, 2011.

[12] Antennas and Propagation Society IEEE, "IEEE standard for definitions of terms for antennas," *IEEE Std 145-2013 (Revision of IEEE Std 145-1993)*, pp. 1–50, Mar. 2014.

[13] W. H. Kummer and E. S. Gillespie, "Antenna measurements-1978," *Proceedings of the IEEE*, vol. 66, no. 4, pp. 483–507, Apr. 1978.

[14] C. Parini, *Theory and Practice of Modern Antenna Range Measurements*, ser. IET Electromagnetic Waves Series. London, U.K.: The Institution of Engineering and Technology, Dec. 2014.

[15] IEEE, "IEEE standard test procedures for antennas," Tech. Rep. IEEE Std 149-1979, 1979.

[16] R. Johnson, H. Ecker, and R. Moore, "Compact range techniques and measurements," *IEEE Transactions on Antennas and Propagation*, vol. 17, no. 5, pp. 568–576, Sep. 1969.

[17] R. C. Johnson, H. A. Ecker, and J. S. Hollis, "Determination of far-field antenna patterns from near-field measurements," *Proceedings of the IEEE*, vol. 61, no. 12, pp. 1668–1694, Dec. 1973.

[18] W. Burnside, M. Gilreath, B. Kent, and G. Clerici, "Curved edge modification of compact range reflector," *IEEE Transactions on Antennas and Propagation*, vol. 35, no. 2, pp. 176–182, Feb. 1987.

[19] E. Joy, W. Leach, and G. Rodrigue, "Applications of probe-compensated near-field measurements," *IEEE Transactions on Antennas and Propagation*, vol. 26, no. 3, pp. 379–389, May 1978.

[20] J. Hansen, *Spherical Near-field Antenna Measurements*, ser. Electromagnetic Waves Series. London, U.K.: Peter Peregrinus Ltd, 1988, no. 26.

[21] 3GPP, "Measurement of radiated performance for Multiple Input Multiple Output (MIMO) and multi-antenna reception for High Speed Packet Access (HSPA) and LTE terminals," 3rd Generation Partnership Project, Technical Report 37.976 V15.0.0, Sep. 2018.

[22] CTIA Certification Program, "Test plan for wireless device over-the-air performance," Washington, DC, USA, Certification Program Test Plan 3.7.1, Feb. 2018.

[23] 3GPP, "Radio frequency (RF) requirement background for active antenna system (AAS) base station (BS)," 3rd Generation Partnership Project, Technical Report 37.842 V13.3.0, Dec. 2019.

[24] P. Kyösti, T. Jämsä, and J.-P. Nuutinen, "Channel modelling for multiprobe over-the-air MIMO testing," *International Journal of Antennas and Propagation*, vol. 2012, May 2012.

[25] 3GPP, "Spatial channel model for multiple input multiple output (MIMO) simulations," 3rd Generation Partnership Project, Technical Report 25.996 V15.0.0, Jun. 2018.

[26] W. Fan, F. Sun, J. Ø. Nielsen, X. Carreño, J. S. Ashta, M. B. Knudsen, and G. F. Pedersen, "Probe selection in multiprobe OTA setups," *IEEE Transactions on Antennas and Propagation*, vol. 62, no. 4, pp. 2109–2120, Apr. 2014.

[27] M. Rumney, R. Pirkl, M. H. Landmann, and D. A. Sanchez-Hernandez, "MIMO over-the-air research, development, and testing," *International Journal of Antennas and Propagation*, Sep. 2012.

[28] M. G. Nilsson, P. Hallbjörner, N. Arabäck, B. Bergqvist, T. Abbas, and F. Tufvesson, "Measurement uncertainty, channel simulation, and disturbance characterization of an over-the-air multiprobe setup for cars at 5.9 GHz," *IEEE Transactions on Industrial Electronics*, vol. 62, no. 12, pp. 7859–7869, Dec. 2015.

[29] M. Rumney, H. Kong, Y. Jing, Z. Zhang, and P. Shen, "Recent advances in the radiated two-stage MIMO OTA test method and its value for antenna design optimization," in *2016 10th European Conference on Antennas and Propagation (EuCAP)*, Apr. 2016, pp. 1–5.

[30] 3GPP, "User equipment (UE) antenna test function definition for two-stage multiple input multiple output (MIMO) over the air (OTA) test method," 3rd Generation Partnership Project, Technical Specification 36.978 V13.2.0, Jun. 2017.

[31] W. Yu, Y. Qi, K. Liu, Y. Xu, and J. Fan, "Radiated two-stage method for LTE MIMO user equipment performance evaluation," *IEEE Transactions on Electromagnetic Compatibility*, vol. 56, no. 6, pp. 1691–1696, Dec. 2014.

[32] W. Fan, P. Kyösti, L. Hentilä, and G. F. Pedersen, "MIMO terminal performance evaluation with a novel wireless cable method," *IEEE Transactions on Antennas and Propagation*, vol. 65, no. 9, pp. 4803–4814, Sep. 2017.

[33] C. Schirmer, M. Lorenz, W. A. T. Kotterman, R. Perthold, M. H. Landmann, and G. D. Galdo, "MIMO over-the-air testing for electrically large objects in non-anechoic environments," in *2016 10th European Conference on Antennas and Propagation (EuCAP)*, Apr. 2016, pp. 1–6.

References

[34] P.-S. Kildal, *Foundations of Antenna Engineering - A Unified Approach for Line-of-Sight and Multipath*, 2015th ed. Gothenburg, Sweden: Kildal Antenn AB, Mar. 2017, available at www.kildal.se.

[35] International Electrotechnical Commission, "Electromagnetic compatibility (EMC) - Part 4-21: Testing and measurement techniques - Reverberation chamber test methods," Tech. Rep. IEC 61000-4-21, 2011.

[36] M. Bäckström, O. Lundén, and P.-S. Kildal, "Reverberation chambers for EMC susceptibility and emission analyses," in *Review of Radio Science: 1999-2002 URSI*. John Wiley & Sons, Aug. 2002, pp. 429–452.

[37] K. Rosengren, P.-S. Kildal, C. Carlsson, and J. Carlsson, "Characterization of antennas for mobile and wireless terminals in reverberation chambers: Improved accuracy by platform stirring," *Microwave and Optical Technology Letters*, vol. 30, no. 6, pp. 391–397, Sep. 2001.

[38] D. Hill, M. Ma, A. Ondrejka, B. Riddle, M. Crawford, and R. Johnk, "Aperture excitation of electrically large, lossy cavities," *IEEE Transactions on Electromagnetic Compatibility*, vol. 36, no. 3, pp. 169–178, Aug. 1994.

[39] C. S. P. Lötbäck, A. Skårbratt, and C. Orlenius, "Extending the reverberation chamber using a channel emulator for characterisation of over-the-air performance of multiple-input-multiple-output wireless devices," *IET Science, Measurement Technology*, vol. 9, no. 5, pp. 555–562, 2015.

[40] CTIA Certification Program, "Test plan for wireless large-form-factor device over-the-air performance," Certification Program Test Plan 1.2.1, Feb. 2019.

[41] J. Kostas and B. Boverie, "Statistical model for a mode-stirred chamber," *IEEE Transactions on Electromagnetic Compatibility*, vol. 33, no. 4, pp. 366–370, Nov. 1991.

[42] P. H. Lehne, K. Mahmood, A. A. Glazunov, P. Grønsund, and P. S. Kildal, "Measuring user-induced randomness to evaluate smart phone performance in real environments," in *2015 9th European Conference on Antennas and Propagation (EuCAP)*, May 2015, pp. 1–5.

[43] P.-S. Kildal, "Preparing for GBit/s coverage in 5G: Massive MIMO, PMC packaging by gap waveguides, OTA testing in random-LOS," in *2015 Loughborough Antennas & Propagation Conference*, Nov. 2015.

[44] P.-S. Kildal, X. Chen, M. Gustafsson, and Z. Shen, "MIMO characterization on system level of 5G microbase stations subject to randomness in LOS," *IEEE Access*, vol. 2, pp. 1062–1075, 2014.

54

[45] P.-S. Kildal, A. A. Glazunov, J. Carlsson, and A. Majidzadeh, "Cost-effective measurement setups for testing wireless communication to vehicles in reverberation chambers and anechoic chambers," in *2014 Conference on Antenna Measurements Applications (CAMA)*, Nov. 2014, pp. 1–4.

[46] P.-S. Kildal, "Methods and apparatuses for testing wireless communications to vehicles," Jan. 2014, patent application number PCT/EP2014/054620. Applicant is Kildal Antenn AB.

[47] A. Razavi, A. A. Glazunov, S. M. Moghaddam, R. Maaskant, and J. Yang, "Characterization method of an automotive random-LOS OTA measurement setup," *Progress In Electromagnetics Research C*, vol. 2018, no. 84, pp. 47–60, 2018.

[48] A. Razavi, A. A. Glazunov, P.-S. Kildal, and J. Yang, "Investigation of polarization deficiencies in SIMO systems in random-LOS propagation channels," in *2015 International Symposium on Antennas and Propagation (ISAP)*, 2015.

[49] A. A. Glazunov, A. Razavi, and P.-S. Kildal, "Simulations of a planar array arrangement for automotive random-LOS OTA testing," in *2016 10th European Conference on Antennas and Propagation (EuCAP)*, Apr. 2016, pp. 1–5.

[50] A. Razavi, A. A. Glazunov, P.-S. Kildal, and R. Maaskant, "Array-fed cylindrical reflector antenna for automotive OTA tests in random line-of-sight," in *2016 10th European Conference on Antennas and Propagation (EuCAP)*, Apr. 2016, pp. 1–4.

[51] R. Haupt, "Generating a plane wave with a linear array of line sources," *IEEE Transactions on Antennas and Propagation*, vol. 51, no. 2, pp. 273–278, Feb. 2003.

[52] D. A. Hill, "A numerical method for near-field array synthesis," *IEEE Transactions on Electromagnetic Compatibility*, vol. EMC-27, no. 4, pp. 201–211, Nov. 1985.

[53] 3GPP, "NR; User equipment (UE) radio transmission and reception; Part 2: Range 2 standalone," 3rd Generation Partnership Project, Technical Specification 38.101-2 V16.3.1, Mar. 2020.

[54] P.-S. Kildal, X. Chen, C. Orlenius, M. Franzén, and C. Patané, "Characterization of reverberation chambers for OTA measurements of wireless devices: Physical formulations of channel matrix and new uncertainty formula," *IEEE Transactions on Antennas and Propagation*, vol. 60, no. 8, pp. 3875–3891, Aug. 2012.